Max-Planck-Institut
für Meteorologie

REPORT No. 178

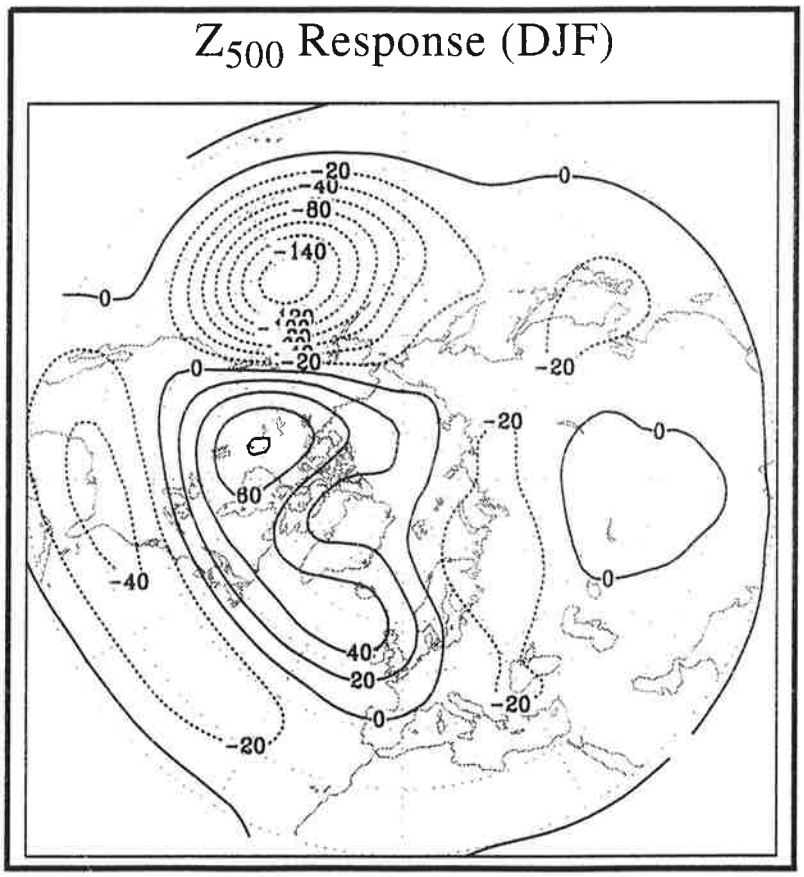

ENSO VARIABILITY AND ATMOSPHERIC RESPONSE IN A GLOBAL COUPLED ATMOSPHERE-OCEAN GCM

by

ERICH ROECKNER · JOSEF M. OBERHUBER · ANDREAS BACHER
MICHAEL CHRISTOPH · INGO KIRCHNER

HAMBURG, November 1995

AUTHORS:

Erich Roeckner
Andreas Bacher
Michael Christoph
Ingo Kirchner

Max-Planck-Institut
für Meteorologie

Josef M. Oberhuber

DKRZ
Deutsches Klimarechenzentrum
Bundesstraße 55
D-20146 Hamburg
F.R.G.

MAX-PLANCK-INSTITUT
FÜR METEOROLOGIE
BUNDESSTRASSE 55
D-20146 Hamburg
F.R. GERMANY

Tel.: +49-(0)40-4 11 73-0
Telefax: +49-(0)40-4 11 73-298
E-Mail: <name> @ dkrz.d400.de

ISSN 0937-1060

ENSO variability and atmospheric response in a global coupled atmosphere-ocean GCM

E. Roeckner[1], J.M. Oberhuber[2], A. Bacher[1], M. Christoph[1], I. Kirchner[1]

[1]Max-Planck-Institut für Meteorologie
[2]Deutsches Klimarechenzentrum
Bundesstraße 55, D-20146 Hamburg, Germany

Abstract

The interannual variability associated with the El Niño/Southern Oscillation (ENSO) cycle is investigated using a high-resolution coupled general circulation model (CGCM) of the atmosphere and ocean. The flux correction is restricted to annual means of heat and freshwater which proved sufficient to prevent the model from drifting to an unrealistic climate state. The annual as well as the seasonal climate in the CGCM is very close to that simulated in the atmospheric model forced with observed sea surface temperatures (SSTs).

During a 100-year simulation of the present-day climate, the model is able to capture many features of the observed interannual SST variability in the tropical Pacific. This applies not only to amplitude, lifetime and frequency of occurrence of El Niño events but also to the phase locking of the SST anomalies to the annual cycle. Although the SST warming during the evolution of El Niños is too confined spatially, and the warming along the Peruvian coast is much too weak, the patterns and magnitudes of key atmospheric anomalies such as westerly wind stress and precipitation, and also their eastward migration from the western to the central equatorial Pacific is in accord with observations. There is also a good correspondence with the results obtained from the atmospheric model forced with observed SSTs 1979 through 1994. The large-scale dynamic response during the mature phase of ENSO (December through February) is characterized by an eastward displacement and weakening of the Walker cell in the Pacific while the Hadley cell intensifies and moves equatorward.

Similar to the observations, there is a high correlation between tropical Pacific SST and the winter circulation in the North Pacific. The deepening of the Aleutian low during the ENSO winters is well captured by the model as well as the cooling in the central North Pacific and the warming over Canada and Alaska. However, there are indications that the anomalies of both SST and atmospheric circulation are overemphasized in the North Pacific. Finally, there is evidence of a coherent downstream effect over the North Atlantic as indicated by a relatively high negative correlation between circulation indices in the North Pacific and North Atlantic, respectively. The weakening of the westerlies across the North Atlantic in ENSO winters which is related to a weakening and southwestward displacement of the Icelandic low, is in broad agreement with the observations, as well as a weak tendency for colder than normal winters in Europe.

ISSN 0937-1060

1 Introduction

The El Niño/Southern Oscillation (ENSO) cycle is the most dominant mode of interannual variability in the atmosphere and in the ocean. Its center of action is in the tropical Pacific, but significant climatic (and societal) impacts have been identified in many regions of the world (Glantz et al., 1991).

As compared to earlier attempts to simulate the ENSO phenomenon in coupled general circulation models (see review by Neelin et al., 1992), some progress has been made in recent years, and most of the current coupled atmosphere-ocean general circulation models (CGCMs) are able to simulate ENSO-like variability that resembles the observed (Lunkeit et al., 1995; Robertson et al., 1995; Schneider et al., 1995; Tett, 1995). In some of these models, the sub-surface memory associated with the propagation of equatorial waves plays a role in maintaining ENSO-like SST fluctuations, and the simulated eastward propagation of heat content anomalies along the equator and westward propagation off the equator is broadly consistent with the delayed action oscillator hypothesis of Suarez and Schopf (1988). Nevertheless, the analysed ENSO mechanisms are not totally consistent with observations, and the amplitude is only half of the observed or less. Consequently, the atmospheric response to ENSO is underestimated in the current CGCMs.

Although no single explanation for ENSO exists, it is recognized that unstable air-sea interactions and equatorial wave dynamics in the upper ocean are important ingredients. Adequate representation of air-sea interaction (Barnett et al., 1991), sufficient coupling strength in the part of the flow which deviates from climatology (Neelin et al., 1992) as well as high resolution in the equatorial wave guide (Philander et al., 1992) have been identified as necessary conditions for realistic ENSO simulations in CGCMs.

This paper focuses on the documentation and validation of the atmospheric ENSO response, in both the tropics and extratropics, as diagnosed from a multi-decadal simulation of the present climate with a high-resolution global CGCM developed at the Max Planck Institute (MPI) in Hamburg. The paper is organized as follows: A brief description of the model and a few examples showing its overall performance are presented in section 2. The model experiments and the observational datasets are described in section 3, the results on ENSO variability and response are presented in section 4, and a discussion of the main findings in section 5 concludes this paper. While the validation of the atmospheric ENSO response is the main theme of this study, the upper ocean variability and annual cycle will be discussed in a companion paper (Bacher et al., 1995).

2 Model description and preliminary validation

2.1 Atmosphere and land surface

The atmospheric component of the CGCM is the 4th generation MPI model (ECHAM-4) which is the most recent in a series evolving from the European Centre for Medium Range Weather Forecasts (ECMWF) model. As the previous ECHAM versions (Roeckner et al., 1992), ECHAM-4 is based on the primitive equations. Prognostic variables are vorticity, divergence, surface pressure, temperature, water vapor and cloud water. Except for the

water components, the prognostic variables are represented by spherical harmonics with triangular truncation at wavenumber 42 (T42). Advection of water vapor and cloud water is treated with a semi-Lagrangian scheme (Williamson and Rasch,1994). A semi-implicit time stepping scheme is employed with a weak time filter. The time step is 24 minutes for dynamics and physics, except for radiation which is calculated at 2-hour intervals. A hybrid sigma-pressure coordinate system is used with 19 irregularly spaced levels up to a pressure level of 10 hPa.

With respect to the previous versions, ECHAM-4 has undergone a number of changes in the physical parameterizations:

1) The radiation code has been adopted from the ECMWF model (Morcrette, 1991) with a few modifications like the consideration of additional greenhouse gases (methane, nitrous oxide and 16 CFCs) and various types of aerosols. Moreover, the water vapor continuum has been revised to include temperature weighted band averages of e-type absorption and also a band dependent ratio of (p-e)-type to e-type continuum absorption (Giorgetta and Wild, 1995). The single scattering properties of cloud droplets and ice crystals are derived from Mie theory with suitable adaptation to the broad-band model (Rockel et al., 1991). The effective radius of droplets and ice crystals is parameterized in terms of the liquid and ice water content, respectively.

2) A high-order closure scheme is used to compute the turbulent transfer of momentum, heat, moisture and cloud water within and above the atmospheric boundary layer. The eddy diffusion coefficients are calculated as functions of the turbulent kinetic energy which is obtained from the respective rate equation (Brinkop and Roeckner, 1995).

3) As in ECHAM-3, the convective mass flux scheme of Tiedtke is applied. However, the closure for deep convection and organized entrainment has been modified and is now based on buoyancy instead of moisture budget, and organized detrainment is computed for a spectrum of clouds detraining at different heights (Nordeng, 1995).

4) As in ECHAM-3, the cloud water content is calculated from the respective budget equation including sources and sinks due to phase changes and precipitation formation by coalescence of cloud droplets and gravitational settling of ice crystals. Different from ECHAM-3, the convective cloud water detrained in cumulus anvils and also in shallow non-precipitating cumulus clouds is used as a source term in the stratiform cloud water equation.

The soil model remained unchanged. It comprises the budgets of heat and water in the soil, the snow pack over land and the heat budget of land ice. Vegetation effects such as the interception of rain and snow in the canopy and the stomatal control of evapotranspiration are parameterized in a highly idealized way. The local runoff scheme is based on catchment considerations and takes into account sub-grid scale variations of field capacity over inhomogeneous terrain. In the coupled model, the hydrological cycle is closed (except for glacier calving which is not taken into account) by a river routing scheme (Sausen et al., 1994) which directs the local runoff into the oceans.

2.2 Ocean and sea ice

The oceanic model component is based on the OPYC model (Oberhuber,1993a,1993b). It consists of three sub-models for the interior ocean, the surface mixed layer and the sea-ice, respectively.

The model for the interior ocean employs the primitive equations in the flux form of the conservation laws for momentum, mass, heat and salt in isopycnal layers. These quantities as well as the sea level are prognostic variables. Horizontal mixing for momentum is a function of the local Rossby deformation radius, while horizontal diffusion for temperature and salinity involves some dependence on flow deformation. Vertical mixing follows the concept of entrainment/detrainment for which budgets of turbulent and mean potential energy are solved. A standard convection scheme is used which instantaneously removes vertical instabilities.

The model for the interior ocean is coupled to a mixed layer model, as the concept of isopycnal coordinates breaks down near the surface when strong turbulence is present. The mixed layer model computes entrainment rates out of an isopycnal layer or detrainment rates into an isopycnal layer according to a budget equation for turbulent kinetic and mean potential energy. Wind stirring, surface buoyancy flux due to heat and fresh water fluxes, sub-surface stability and flow shear enter the calculation.

The sea-ice model solves for ice momentum, ice and snow thickness and their concentration. The viscous-plastic rheology is chosen to parameterize the stress tensor while the thicknesses of ice and snow and the concentration of ice are computed from the respective continuity equations. Further parameterizations relate heat fluxes to changes in ice and snow thickness as well as lead size and to changes in salinity due to brine rejection. Moreover, the conversion from snow to ice as due to snow aging and snow suppression is included in parametric form. The thermodynamic part consists of a prognostic computation of the temperature profile, taking into account the heat capacity and conductivity of the slab and the net surface heat flux.

The governing equations are solved on an Arakawa B-grid with no-slip horizontal boundary conditions. A fully implicit time stepping scheme is employed as well as an alternating direction implicit (ADI) solution technique. Poleward of 36°, the horizontal resolution is identical to that of the atmospheric model (~2.8°, identical to the T42 Gaussian grid). At low latitudes, to allow for a better representation of the equatorial wave guide, the meridional grid spacing is gradually decreased down to 0.5° at the equator. Vertically, 11 layers have been chosen.

2.3 The coupled model

Prior to coupling, the OGCM has been spun up for about 1000 years by prescribing a combination of observed and AGCM simulated fluxes and variables. While the dynamical components such as wind stress and friction velocity have been derived from the AGCM forced with observed climatological sea surface temperatures (SSTs), the fluxes of heat and freshwater are based on a combination of (i) observed climatology (Oberhuber, 1988), (ii) a bulk flux parameterization and (iii) additional relaxation towards observed SSTs (AMIP climatology) and surface salinity (Levitus, 1982), respectively.

The drift induced by the 'coupling shock' when the restoring boundary conditions are replaced by the fluxes computed in the CGCM can be reduced considerably if flux correction (or adjustment) techniques are applied (e.g., Sausen 1988). However, the methods which have been employed so far are not totally satisfactory since the SST still tends to drift by typically 0.5K in the global mean within the first 100 years after coupling (Cubasch et al., 1992; Lunkeit et al., 1995). It is also contended by some modeling groups (see Neelin et al., 1992) that the seasonal correction, particularly if SST itself undergoes a correction independent from the heat flux (Lunkeit, 1995), tends to reduce and/or spectrally modify ENSO variability. In the current model, an alternative approach (Bacher and Oberhuber, 1995) is applied. It differs from the traditional one basically in two aspects, namely, (i) the flux correction is computed by gradual updating during a 100-year spinup of the CGCM, and (ii) only the annual mean of heat and freshwater is corrected while the respective annual cycles and the wind stress altogether (and all other coupling variables as well) remain unchanged.

After the CGCM spinup, the model has been integrated for another 100 years with the flux correction fixed in time. In this present-day control experiment, a relatively small secular drift is found with a cooling trend of the ocean (all layers) of about 0.1K, a freshening of the upper ocean by typically 0.02 psu and a salinity increase with about the same rate in the deep ocean. As an example, Fig. 1 shows the evolution of surface air temperature during the first 100 years of the control experiment. Superimposed upon a weak cooling trend, similar to that of the ocean, are interannual and interdecadal fluctuations with approximately the same amplitude as those seen in the observational record during the last 100 years (IPCC, 1990; Fig. 7.10).

Due to the flux correction, the annual mean SST distribution simulated in the CGCM is very close to that obtained during the OGCM spinup. As compared to the observations, the annual mean SST deviations are generally below 1°C. Larger errors (in both the OGCM and CGCM) are found in the regions of the western boundary currents which are not sufficiently resolved by the model. However, since these large errors are confined to a small area, the impact on the climate of the atmosphere is insignificant. This applies not only to the global mean variables, which are reasonably close to those simulated with the AGCM driven with observed SSTs (Table 1), but also to the regional distributions. Figure 2 shows a comparison of annual mean precipation as simulated with the CGCM and AGCM, respectively. Although precipitation is one of the climate variables which is known to respond sensitively to SST changes, its large scale distribution in the CGCM appears to be rather close to that of the AGCM, and this applies for the other climate variables as well.

Since the annual cycle is not modified, the SST errors are expected to be larger in the individual seasons than in the annual mean. Again the largest seasonal SST errors occur in the regions of the western boundary currents with maximum values during winter of up to 5K at individual gridpoints off Newfoundland and Japan. Similar to the annual mean climate, the seasonal climate is hardly affected because the spatial extent of these relatively large errors is small. As an example, Fig. 3 shows that the error distribution of DJF sea level pressure obtained from the CGCM is very similar to that of the AGCM driven with observed SST. Since this applies to the other climate variables and seasons as well,

we conclude that the systematic errors of the CGCM reflect those of the AGCM rather than errors in the SST distribution.

Table 1: Global annual mean climate variables as simulated in the CGCM and AGCM (ECHAM-4), respectively. The averaging period is 100 y for the CGCM and 30 y for the AGCM. The last two columns refer to top-of-atmosphere longwave and shortwave radiative fluxes with the respective cloud forcings added in brackets.

	Sfc. air temp. (°C)	Precip (mm/d)	Column water vapor (kg/m^2)	Column cloud water (g/m^2)	Total cloud cover (%)	Net SW radiation [SWCF] (W/m^2)	Net LW radiation [LWCF] (W/m^2)
CGCM	14.7	2.82	24.5	78.8	59.8	237.9 [- 49.9]	- 235.7 [28.9]
AGCM	14.4	2.81	24.4	78.9	59.8	236.9 [- 49.3]	- 235.3 [28.8]

3. Model experiments and observational data

In the CGCM experiment, the solar constant as well as the concentrations of atmospheric greenhouse gases are prescribed according to current conditions (IPCC, 1990). Moreover, since both the OGCM spinup and the compution of the flux correction are based on the currently observed SST distribution, the CGCM experiment can be considered as a simulation of the present-day climate. This so-called control experiment (reference for future scenario experiments) has been initialized at year 90 (!) of the 100y coupled spinup run. However, the flux correction used in the control run is based on the full 100y spinup, so that there is an overlap of 10 years between both runs.

In addition to this CGCM control experiment, two Atmospheric Model Intercomparison Project (AMIP)-type experiments (Gates, 1992) have been performed using the atmospheric component of the CGCM (ECHAM-4). In these experiments, observed monthly mean SSTs and sea ice extents (Jan '79 through May '94) are prescribed according to an extended AMIP SST and sea ice dataset. The experiments differ only with respect to the initial conditions.

In addition to AMIP, the so-called GISST (Global Ice Sea Surface Temperature; Parker et al., 1994) dataset covering the period 1949-91 is used for CGCM validation. Although it is is available on a 1°x1° grid, its effective resolution is coarser because the SST field has been created by adding 5° resolution anomalies to a 1° resolution climatology.

Operational ECMWF analyses (1980-1994) of sea level pressure, geopotential height, wind and temperature are used as an observational reference for the simulated atmospheric response to ENSO.

4 ENSO variability and atmospheric response

4.1 Tropics

The comparison between the observed and simulated time series of monthly SST anomalies (SSTA) in the eastern tropical Pacific (Fig. 4) shows that the CGCM is able to simulate a realistic level of interannual variability. Very strong El Niños occur especially during the last 30 years with anomalies of up to 3K as in the observed 1982-83 event. There are also suppressed periods with anomalies of less than 1K for about one decade (years 104-113 and 151-159, respectively). In this study, El Niño events are identified according to amplitude (SSTA≥1K, indicated by the dashed line in Fig. 4) and persistence (SSTA>0 for at least one year) of NINO3 SSTA. According to this definition, 11 events are identified during the 43y-period 1949-91 (Fig. 4a) with onsets during 1951, 1953, 1957, 1963, 1965, 1969, 1972, 1976, 1982, 1986 and 1991. In the simulation (Fig. 4b), El Niños are less frequent than observed during the first 50 years (11 events: years 91,93, 99, 102, 114, 117, 119, 121, 125, 131, 138), but occur more often during the last 50 years (14 events: years 143, 145, 147, 149, 160, 162, 164, 167, 171, 173, 176, 178, 182, 189). During the 100 y control run, the mean distance between two events is 4 years, which is not only similar to that analysed from the GISST dataset but also to the analysis of historical El Niños (1800-1986) by Quinn et al. (1987) who found a mean distance of 3.8 years if 'very weak' events were excluded. As already apparent from a visual inspection of the time series, the biennual mode is more pronounced in the model than in the observations. A spectral analysis of the model data shows two significant peaks around 2 and 4 years, respectively, while for the GISST data a significant peak between 3 and 3.5 years is found (not shown).

The evolution of SST and other key climate parameters during ENSO is studied by means of ensemble averaging all El Niño events that have been identified according to the definition given above. These years will be called EN-years. The year following EN is called post-El Niño year (PEN) while all other years form the ensemble of non-El Niño years (NEN). The mean El Niño response is defined as the difference of the respective climate parameter between the ensemble of EN years and NEN years, respectively. Although each event is different and a 'canonical' El Niño does not exist, this compositing technique offers a convenient way to study the gross features of ENSO. So far, only years 90-140 have been analysed in detail, and all of the CGCM composites discussed in this paper refer to this 50y period.

The evolution of the CGCM simulated and GISST observed monthly mean composite SSTA along the equatorial belt is shown in Fig. 5a,b for the EN and PEN years, respectively. The AMIP SSTA composite which is based on the 1979-94 subset is shown in addition (Fig. 5c), in order to facilitate the interpretation of the ECHAM-4 simulated and ECMWF observed response to which this period applies. Although the observed SSTA evolution of the full ensemble is similar to that of the AMIP subset, we note also differences. Firstly, the initial warming along the Peruvian coast which often occurred prior to 1980 (Rasmussen and Carpenter, 1982), was either weak or non-existent during the later events. Secondly, the events of 1982-83 and 1986-87 maintained large anomalies throughout the PEN years 1983 and 1987 (according to our definition). Some of the differences between the ENSO responses in the CGCM, the ECMWF analyses and the

AGCM driven with AMIP-SST, respectively, that will be discussed in the following figures can be attributed to the 'anomalous ' SSTA evolution during the AMIP period, particularly in the PEN years.

In the model simulation, the warming lasts for one year on average with a rather abrupt onset during the spring of the EN year and a rather rapid decay one year later, similar as in the GISST dataset. Maximum values of more than 2K around 110°W are simulated and observed during November and December of the EN year. However, there are also unrealistic features in the model simulation, for example, (i) the warming in the central Pacific is underestimated especially during the mature phase and the warming in that area starts to retreat too early, (ii) the coastal warming is too weak during the first half of the EN year and (iii) the onset as well as the decay of the 'mean' El Niño is too abrupt which indicates less variability within the CGCM ensemble than in the observed and possibly a too tight phase locking to the annual cycle.

In the following figures we show the evolution of several key climate variables during the EN and PEN years, respectively, as simulated with the CGCM. We also discuss the results obtained from the AGCM driven with AMIP-SSTs and observational estimates according to ECMWF analyses as well. However, as explained above, these results cannot be used as a true reference for a quantitative validation of the CGCM simulation.

Traditionally, the atmospheric part of the ENSO cycle is described by a near-global seesaw of sea level pressure (SLP) with centers of action located over Indonesia and the tropical South Pacific (e.g., Trenberth and Shea, 1987). During El Niño events the SLP over the anomalously warm waters in the tropical East Pacific is relatively low while it is relatively high over the tropical West Pacific, i.e. the pressure gradient across the tropical Pacific is weaker than during normal conditions. This feature is evident from Fig. 6 which shows the evolution of composite equatorial SLP anomalies during the EN and PEN years. A comparison of Figs. 6a with 5a and 6b,c with 5c, respectively, indicates the expected out-of-phase relationship between SST and SLP.

Consistent with the diminished zonal pressure gradient, particularly in the central equatorial Pacific, is the evolution of westerly wind-stress anomalies (Fig. 7). During the first half of the EN year, the anomalies migrate eastward from the western to the central Pacific where they attain their largest values. This behavior is consistent with the observed evolution of near-equatorial surface wind anomalies during El Niño years (Pazan and Meyers, 1982; Rasmussen and Carpenter, 1982). It is interesting to note that both the CGCM and the AGCM are able to simulate the southward shift of the westerly wind anomalies across the equator (not shown) observed during the mature phase between November and January (Harrison, 1987). In the CGCM, maximum westerly wind-stress anomalies of about 0.05 Pa (DJF composite) are generated at 5°S,170°W which corresponds well with the observed westerly wind anomalies of 4 m/s at about the same location for an ensemble of 7 El Niños during 1953-77. In agreement with observations also, the westerly anomalies do not extend into the far eastern Pacific. Even during the mature stage they are confined to the region westward of about 130°W (Rasmussen and Carpenter, 1982).

The precipitation anomalies (Fig. 8) evolve almost in phase with the wind-stress anomalies in the region of enhanced low-level convergence to the west of the maximum

SST anomalies. The pattern evolution as well as the amplitude of more than 10 mm/d are similar to that derived from satellite observations (Fennessy and Shukla, 1988; Janowiak and Arkin, 1991). Moreover, since also the model responses are similar (except during PEN years; see above), we conclude that the forcing of the equatorial troposphere by anomalous latent heat release in the central Pacific during EN years is realistically captured by the CGCM with respect to both magnitude and location.

The mid-tropospheric latent heat release is a crucial element in a positive feedback loop triggered by positive SSTA through anomalous moisture convergence and rising motion which both tend to maintain the latent heat release in the central Pacific (Barnett et al., 1991). This positive feedback is amplified by the formation of thick cirrus anvils which contribute to the total diabating heating anomaly through trapping of upwelling infrared radiation (Sherwood et al., 1994; Lohmann and Roeckner, 1995). Associated with the shift of the major convective center from the western to the central Pacific is a shift of the Walker cell which can be identified in Fig. 9 by the upper tropospheric easterly wind anomalies in the central and eastern Pacific. Although the pattern evolution is similar, the anomalies simulated in CGCM are consistently smaller than those obtained from the AGCM simulation and ECMWF analyses during the AMIP period. This applies also to the westerly anomalies at 850 hPa (not shown) with peak values of 4 m/s in the CGCM composite as compared to 6 m/s in the AGCM and ECMWF analyses, respectively. In general, the dynamical response to the tropical SSTA simulated in the coupled model is not only similar to the observed but also consistent with that obtained from linear models (e.g., Gill, 1980).

4.2 Extratropics

Many observational studies have demonstrated the impact of El Niño events on the extratropical circulation, particularly during the northern hemisphere winter (e.g., Horel and Wallace, 1981; van Loon and Madden, 1981; Hamilton, 1988; Fraedrich, 1994). Moreover, numerous modeling studies with AGCMs forced with observed SSTs have been performed which not only captured many essentials of the observed response but even showed some predictive skill (Bengtsson et al., 1993; Barnett et al., 1994; Palmer and Anderson, 1994). On the other hand, extratropical response studies with CGCMs are rather limited (Meehl, 1991), probably due to the relatively weak El Niños simulated in the current models.

The teleconnection between tropical Pacific SSTA and the winter circulation in the North Pacific has been noted already by Bjerknes (1969) among others. In the coupled model, the close link between ENSO and the extratropical circulation is evident in the time series of various indices shown in Fig. 10. The Southern Oscillation index (SOI) is defined here as the difference between the SLP at Tahiti and Darwin (nearest grid points) normalized by the respective standard deviations. The PNA index is constructed, analogous to Wallace and Gutzler (1981), by a linear combination of normalized 500 hPa height anomalies z^* at the grid points nearest to the four PNA centers of the CGCM. The position of these centers, as identified from the CGCM teleconnectivity map, are slightly different to those obtained by Wallace and Gutzler for an observational record of 45 winter months (DJF 1962-63 through 1976-77). Accordingly, the index used here is defined as

$$PNA = \{z^*[12°N,163°W] - z^*[40°N,149°W] + z^*[60°N,101°W] - z^*[29°N,90°W]\}/4 \quad (1)$$

The ENSO time series shows the expected negative correlation between NINO3 SST and the SOI (Fig. 10a). Although the ENSO mode of variability is clearly dominant, there are also indications for interdecadal variations such as a positive SOI index and a relatively cold tropical East Pacific throughout a decade (years 150 to 160). Oppositely, the tropical East Pacific is relatively warm and the SOI mostly in the negative phase during the preceding decade, not unlike the persistent warming observed during the 1990s. However, the decadal mode identified from observations has a horseshoe-like signature with the strongest SST anomalies in the western equatorial Pacific, extending to the northeast and southeast (Latif et al., 1995), while the decadal anomalies in our CGCM are more ENSO-like (not shown).

Table 2: Simulated (CGCM) and observed (OBS) correlations (coefficients x 100) between time series of various indices (see text and Fig. 10). For the model, maximum correlations are given with respect to the lag in months denoted by the values in brackets, while contemporaneous correlations are given for the observations according to Horel and Wallace (1981).

	SOI (SLP Tahiti-Darwin) vs. NINO3-SST	PNA-index vs. NINO3-SST	PNA-index vs. SOI	PNA-index vs. NAO-index
CGCM	- 75 (0)	78 (2)	- 64 (2)	- 55 (0)
OBS	- 83 (0)	46 (0)	- 31 (0)	

Most of the simulated ENSO events can also be identified through a positive PNA index (Fig. 10b) which is highly correlated with the NINO3 index. Actually, according to Table 2, this correlation is higher in the model than in the observations while the opposite holds for the ENSO indices. However, we have to note that the observed correlations have been obtained for the winter months only while the simulated ones are based on the full time series. Figure 10b and Table 2 also show a relatively high correlation between the PNA index and the North Atlantic Oscillation (NAO) index which is defined here, analogous to Hurrell (1995), as the normalized SLP difference between the grid points nearest to Lissabon and Stykkisholmur (Iceland). Hence, the NAO index is a measure for the strength of the surface westerlies across the North Atlantic. The positive correlation between the NINO3 and the PNA indices, on the one hand, and the negative correlation between PNA and NAO, on the other hand, indicates not only the expected strengthening of the Aleutian low during El Niño years but also a weakening of the westerlies across the North Atlantic.

Figure 11 shows the spatial patterns of the simulated and observed SSTA during the mature phase of ENSO. As already discussed above (cf., Fig. 5), the simulated anomalies

are larger than observed in the eastern equatorial Pacific but smaller in its central part. Also, the meridional extent is smaller than in the observations. Although the simulated global SSTA pattern is similar to that analysed from the GISST dataset, the contributon from ENSO is not known. One exception is certainly the North Pacific pattern which is forced by ENSO through atmospheric teleconnections (e.g., Luksch and von Storch, 1992; Deser and Blackmon, 1995). This pattern is well simulated by the model but the amplitude is larger than in both of the observational datasets.

The DJF precipitation response is shown in Fig. 12. Both the CGCM and the AGCM-AMIP simulate positive anomalies throughout the equatorial Pacific with peak values of more than 10 mm/d in its central part (cf., Fig. 8). In the AGCM, the positive anomalies extend further into the Indian Ocean. The tropical Pacific pattern with negative anomalies both northward and southward of the positive anomaly are indicative of an equatorward shift of the Intertropical Convergence Zone (ITCZ) and South Pacific Convergence Zone (SPCZ), respectively, which tend to merge into a huge convective complex centred at the equator during the mature phase of ENSO. Associated with the shift of the convection zone is a weakening and eastward displacement of the Walker cell, while the Hadley cell moves towards the equator and intensifies.

Although the observational database of precipitation is limited, with large gaps especially over the oceans, there are many indications that the simulated response pattern is broadly consistent with observations (Ropolewski and Halpert, 1987). At least, there is qualitative agreement between the models and the observations with respect to regions of coherent negative (Indonesia, Australia, northeastern South America) and positive anomalies (Gulf of Mexico, Southern United States). On the other hand, the observed relative wetness over equatorial East Africa is not captured by the models while the wetness along the Californian coast is too pronounced in both simulations. During JJA of the EN years (not shown), both models simulate a negative precipitation anomaly over the Indian subcontinent, in qualitative agreement with observations (Ropolewsi and Halpert,1987; Shukla, 1991). The dryness over India is related to a general weakening of the Indian summer monsoon in the EN ensemble, as indicated, for example, by the Somalijet and the tropical easterly jet which are both weaker in the simulations than under normal conditions.

The most robust extratropical response to tropical Pacific SSTA is observed in the North Pacific. In winter, the Aleutian low is deeper in El Niño years than under normal conditions and often displaced southeastward towards the North American coast (Bjerknes, 1969; Namias, 1976; van Loon and Madden, 1981). This feature is clearly evident in the simulated and observed SLP response shown in Figure 13. The deepening of the Aleutian low is more pronounced in the CGCM (Fig. 13a) than in the AGCM simulation (Fig. 13b) or ECMWF analyses (Fig. 13c). The CGCM response is also larger than that obtained by van Loon and Madden (1981, Fig. 5) from a long observational record of 80 years. Since the tropical forcing in the CGCM is not overly strong as compared to the AGCM (cf. Figs. 8 and 12), local air-sea interactions could play a role as indicated by the relatively large SST cooling in the central North Pacific (Fig. 11a). This cooling is the result of cold and dry northerly flow along the western flank of the SLP anomaly together with anomalous upwelling due to cyclonic shear, while the warming along the North American coast is caused by advection of warm and humid air and coastal downwelling due to the prevailing

southerly wind anomalies (e.g., Luksch and von Storch, 1992). Unstable air-sea interaction has been identified as an important component of interdecadal variability in the North Pacific (Latif and Barnett, 1994). It remains to be seen, by suppressing possible feedbacks between SST and atmospheric circulation in the uncoupled AGCM forced with the SSTA of the CGCM, if unstable air-sea interactions are important also for shorter time scales.

Relatively good agreement between the simulated and observed SLP responses is found also in the North Atlantic. A similar pattern, but shifted to the north by about 10°, has been analysed also from observations (van Loon and Madden, 1981; Hamilton, 1988). Hence, the simulated impact of ENSO on the North Atlantic Oscillation (see also Table 2) is broadly consistent with the observations which indicate weaker westerlies across the Atlantic during the respective winter months.

The 500 hPa geopotential height response shown in Fig. 14 is very similar to the SLP response discussed above. There is hardly any tilt in the vertical axes of the anomalies but the amplitudes increase with height. The CGCM response, in particular, is dominated by a PNA-like pattern. Although the PNA oscillation is an eigenmode of the atmosphere which is also generated in models forced with climatological SSTs (e.g., Bengtsson et al., 1995), its phase is largely determined by tropical SSTA (cf. Table 2). Some of the discrepancies between the simulated and observed patterns, such as the negative anomaly to the west of Greenland found in the ECMWF analyses but not in the simulation can probably be attributed to the small sample size (3 EN events in the ECMWF analyses). Due to the large internal variability of the extratropical winter circulation in the northern hemisphere (Palmer and Anderson, 1994; Bengtsson et al., 1995), a sample size of 3 EN events is definitely too small for analysing the details of the remote response. In addition to that, the observed EN ensemble also includes external effects such as those induced by the volcanic eruptions of El Chichón in 1982 and Pinatubo in 1991 which may have perturbed the ENSO signal (Kirchner and Graf, 1995; Robock and Mao, 1995).

The temperature response at 850 hPa (Fig. 15) has a PNA-like structure which is consistent with the response in the mass fields shown above (cf., Figs. 13, 14). Similar to the SSTA pattern (Fig. 11), the CGCM simulates a pronounced atmospheric cooling in the eastern part of the North Pacific while the observed cooling is more widespread over the whole North Pacific. A substantial warming during ENSO winters is simulated and observed over Canada and Alaska while the southern part of the U.S. is slightly colder than under normal conditions. A unique feature in the ECMWF analyses is the cold anomaly over Greenland which is captured by none of the models (see discussion of Fig. 14). In both model simulations, parts of Europe are slightly cooler than normal due to the weaker westerlies in the North Atlantic during the ENSO winters (cf., Fig. 13). This feature is not supported by the ECMWF data. However, from an analysis of a long observational record, Fraedrich and Müller (1992) were able to identify a cooling pattern during El Niño winters and a warming during La Niña winters with the respective maxima centred over Scandinavia. Hence, in order to identify such a relatively weak signal, a large sample size is required and, in the observations, appropriate filtering of the volcanic signal which tends to obscure the ENSO signal (Robock and Mao, 1995).

5 Discussion and concluding remarks

We have attempted to validate the interannual variability in the atmosphere as generated in a multi-decadal simulation of the current climate with a high-resolution global CGCM consisting of the components ECHAM-4 and OPYC-3. We have focused on the ENSO related part of the variability within the tropics and on the extratropical response of the northern hemisphere winter circulation. Although we have not addressed the issue of pattern significance, there are many indications that the model might be able to simulate not only a realistic level of tropical ENSO variability but also a remote response which is dynamically consistent and in good agreement with observations as well.

In particular, consistent with the observations, there is a high correlation between tropical Pacific SST and the winter circulation in the North Pacific with a lag of about two months. Moreover, there is evidence of a coherent downstream effect over the North Atlantic as indicated by a relatively high negative correlation between circulation indices in the North Pacific (PNA pattern) and the North Atlantic (NAO). The weakening of the westerlies across the North Atlantic in ENSO years, resulting from a weakening and southwestward shift of the Icelandic low, is in broad agreement with the observations, as well as the tendency for colder than normal winters in Europe. However, the latter signals are much weaker than those found over the North Pacific and North America, and a large sample size is necessary in order to unequivocally isolate them from the high noise level at these latitudes. The good agreement between simulated and observed ENSO induced interannual variability, with respect to both amplitude and pattern, will increase the confidence in the results of climate change experiments planned with this model, particularly with respect to the pattern of regional climate change.

Despite these encouraging results, there are a number of points in which the model deviates from the observations, for example:

(1) Although both amplitude and frequency of El Niño events are realistically captured in general, the model tends to overemphasize the biennual component. This is not only evident from a spectral analysis but also from the temporal evolution of the SSTA composite which indicates a rather abrupt transition between warm and cold phases during the respective spring season. The lifetime of the events is very close to one year on average, and there is a very tight phase locking to the annual cycle. In the observations, the variability within the sample is larger with respect to both lifetime and time of onset. Consequently, the temporal evolution of the composite is 'smoother' than in the simulation.

(2) The simulated SSTA pattern resembles the observed, but the meridional and latitudinal SSTA gradients are larger than observed. While the local maximum in the East Pacific is larger than observed, the coastal warming is much too weak, in particular during the initial stages of El Niño. However, its impact on the atmospheric response is expected to be minor because the dynamic and thermodynamic interactions between the ocean and the atmosphere, as indicated by the evolution of wind stress and precipitation anomalies, for example, are much more important westward of the maximum SSTA in the central equatorial Pacific.

(3) There are indications that the anomalies of both SST and atmospheric circulation are overestimated in the North Pacific during the ENSO winters. The central Pacific SST cooling and the corresponding warming along the Californian coast are both larger than observed. This feature is dynamically consistent with the atmospheric circulation anomalies which are larger than observed as well. Since the tropical forcing in the CGCM is not overly strong and, in fact, smaller than in the AGCM experiment with prescribed observed SSTs, the amplification can only be understood from local air-sea interactions. Small errors in the oceanic response are possibly amplified through positive feedbacks involving processes in the atmosphere and the ocean. Uncoupled AGCM experiments with SSTA prescribed from the coupled model are planned for further clarification. Alternative interpretations would be (i) less event-to-event variability within the ensemble of simulated ENSO winters than in the observations, (ii) insufficient sample size of the observational records used for validation or (iii) poor data coverage in the North Pacific area.

Although ENSO-like variability is simulated in virtually all of the current-generation CGCMs, the present model stands out (to our knowledge) because it is able to simulate a realistic amplitude of tropical Pacific SST variability and, hence, a realistic atmospheric variability as well. Although a thorough discussion of possible reasons is not within the scope of this paper, we conclude by summarizing a few possible candidates. First, the model has a relatively high horizontal resolution of T42 globally, and there is a further low-latitude refinement of the ocean grid down to 0.5° at the equator so that equatorial waves are reasonably well resolved. As compared to the low-resolution (T21) CGCMs employed so far at MPI (Cubasch et al., 1992; Lunkeit et al., 1995), the wind stress in the tropics is almost doubled in the current model and is within the range of observational uncertainty, so that a flux correction of wind stress is no longer necessary. Second, due to the use of isopycnal coordinates in the ocean model, the tropical thermocline is well simulated (Bacher et al., 1995) while in more conventional models the thermocline is often too diffusive due to a combination of coarse vertical resolution and numerical diffusion. Finally, in the atmospheric model, the closure in the convection scheme is no longer based on the moisture budget as in the previous MPI models (and many other CGCMs as well) but on convective instability. Hence, in the tropics, precipitation and latent heat release is more closely linked to SST which results in a realistic representation of the tropical convergence zones such as the ITCZ and the SPCZ, in particular (c.f., Fig. 2). Models employing a moisture convergence closure, on the other hand, generally underestimate the SPCZ and tend to produce a double ITCZ structure in the Pacific separated by a cold and dry equatorial tongue that extends too far to the west (e.g., Latif et al., 1994; Slingo et al., 1994). Furthermore, as shown by Nordeng (1995), the buoyancy closure produces a higher and more realistic level of transient kinetic energy in the tropical West Pacific. Hence, not only the mean state is improved with the new scheme but also the high-frequency variability in the tropics. To what extent these features are crucial for ENSO is still an open question.

Another open question refers to flux correction techniques. Although these methods have their merits in improving the mean climate state in coupled models, an unwanted impact on variability cannot be ruled out. In the present model, the flux correction is restricted to annual means of heat and freshwater which proved sufficient to prevent the model from

drifting to an unrealistic climate state. The correction of the annual mean instead of the annual cycle aims at minimizing its influence on variability.

Acknowledgements.

The authors wish to thank Lennart Bengtsson for continual encouragement and helpful discussions during the course of this work. This research was supported by the project 'Klimavariabilität und Signalanalyse' of the Bundesminister für Bildung und Forschung (BMBF) under grant 07VKV01/1.

References

Bacher A, Oberhuber JM (1995) Global coupling in the ECHAM4/OPYC3 atmosphere-sea ice - ocean GCM with annual mean flux correction restricted to heat and freshwater. In preparation.

Bacher A, Oberhuber JM, Roeckner E (1995) ENSO dynamics and seasonal cycle in the tropical Pacific as simulated by the ECHAM4/OPYC3 coupled general circulation model. Clim Dyn (submitted)

Barnett TP, Latif M, Kirk E, Roeckner E (1991) On ENSO physics. J Climate 4: 487-515

Barnett TP, Bengtsson L, Arpe K, Flügel M, Graham N, Latif M, Ritchie J, Roeckner E, Schlese U, Schulzweida U, Tyree M (1994) Forecasting global ENSO-related climate anomalies. Tellus 46A: 381-397.

Bengtsson L, Schlese U, Roeckner E, Latif M, Barnett TP, Graham NE (1993) A two-tiered approach to long-range climate forecasting. Science 261: 1026-1029

Bengtsson L, Arpe K, Roeckner E, Schulzweida U (1995) Climate predictability experiments with a general circulation model. Clim Dyn (submitted)

Bjerknes J (1969) Atmospheric teleconnections from the equatorial Pacific. Mon Wea Rev 97: 163-172

Brinkop S, Roeckner E (1995) Sensitivity of a general circulation model to parameterizations of cloud-turbulence interactions in the atmospheric boundary layer. Tellus 47A: 197-220.

Cubasch U, Hasselmann K, Höck H, Maier-Reimer E, Mikolajewicz U, Santer BD, Sausen R (1992) Time-dependent greenhouse warming computations with a coupled ocean-atmosphere model. Clim Dyn 8: 55-69

Deser C, Blackmon ML (1995) On the relationship between tropical and North Pacific sea surface temperature variations. J Climate 8: 1677-1680

Fennessy MJ, Shukla J (1988) Numerical simulation of the atmospheric response to the time varying El Niño SST anomalies during May 1982 through October 1983. J Climate 1: 195-211

Fraedrich K (1994) An ENSO impact on Europe? A Review. Tellus 46A: 541-552.

Fraedrich K, Müller K (1992) Climate anomalies in Europe associated with ENSO extremes. J Climatol 12: 25-31

Gates WL (1992) The Atmospheric Model Intercomparison Project. Bull Amer Met Soc 73: 1962-1970

Gill AE (1980) Some simple solutions for heat-induced tropical circulation. Quart J Roy Met Soc 106: 447-462

Giorgetta M, Wild M (1995) The water vapour continuum and its representation in ECHAM-4. Max-Planck-Institut für Meteorologie, Report No. 162, Hamburg, FRG

Glantz MH, Katz RW, Nicholls N (eds) (1991) Teleconnections linking worldwide climate anomalies: Scientific basis and societal impact. Cambridge University Press, 535 pp

Hamilton K (1988) A detailed examination of the extratropical response to tropical El Niño/ Southern Oscillation events. J Climatol 8: 67-86

Harrison DE (1987) Monthly mean island surface winds in the central tropical Pacific and El Niño events. Mon Wea Rev 115: 3133-3145

Horel JD, Wallace JM (1981) Planetary-scale atmospheric phenomena associated with the Southern Oscillation. Mon Wea Rev 109: 813-829

Hurrell JW (1995) Decadal trends in the North Atlantic Oscillation and regional temperature and precipitation. Science 269: 676-679

IPCC (1990) Climate Change, The IPCC Scientific Assessment. JT Houghton, GJ Jenkins, JJ Ephraums (eds) Cambridge University Press, 364 pp.

Janowiak JE, Arkin PA (1991) Rainfall variations in the tropics during 1986-1989, as estimated from observations of cloud-top temperature. J Geophys Res 96: 3359-3373

Kirchner I, Graf H-F (1995) Volcanoes and El Niño: Signal separation in Northern Hemisphere winter. Clim Dyn 11: 341-358

Latif M, Barnett TP (1994) Causes of decadal climate variability over the North Pacific and North America. Science 266: 634-637.

Latif M, Stockdale T, Wolff J, Burgers G, Maier-Reimer E, Junge MM, Arpe K, Bengtsson, L (1994) Climatology and variability in the ECHO coupled GCM. Tellus 46A: 351-366.

Latif M, Kleeman R, Eckert C (1995) Greenhouse warming, decadal variability, or El Niño? An attempt to understand the anomalous 1990s. Max-Planck-Institut für Meteorologie, Report No 175, Hamburg, FRG

Levitus S (1982) Climatological atlas of the world ocean. NOAA Professional Paper No. 13, US Govt Printing Office, Washington DC

Lohmann U, Roeckner E (1995) Influence of cirrus cloud radiative forcing on climate and climate sensitivity in a general circulation model. J Geophys Res 100: 16305-16323

Lunkeit F, Sausen R, Oberhuber JM (1995) Climate simulations with the global coupled atmosphere-ocean model ECHAM2/OPYC. Part I: present-day climate and ENSO events. Clim Dyn (submitted)

Luksch U, von Storch H (1992) Modeling the low-frequency sea surface temperature variabiity in the North Pacific. J Climate 5: 893-906.

Meehl GA (1991) The Southern Oscillation in a coupled GCM: Implications for climate sensitivity and climate change. In 'Greenhouse-gas induced climatic change: A critical appraisal of simulations and observations' (ME Schlesinger, ed). Developments in Atmospheric Sciences 19: 111-128, Elsevier.

Morcrette JJ (1991) Radiation and cloud radiative properties in the European Centre for Medium Range Weather Forecasts forecasting system. J Geophys Res 96: 9121-9132

Namias J (1976) Some statistical and synoptic characteristics associated with El Niño. J Phys Oceanogr 6: 130-138

Neelin JD, Latif M, Allaart MAF, Cane M, Cubasch U, Gates WL, Gent PR, Ghil M, Gordon C, Lau NC, Mechoso NC, Meehl GA, Oberhuber JM, Philander SGH, Schopf PS, Sperber KR, Sterl A, Tokioka T, Tribbia J, Zebiak SE (1992) Tropical air-sea interaction in general circulation models. Clim Dyn 7: 73-104

Nordeng TE (1995) Extended versions of the convective parameterization scheme at ECMWF and their impact on the mean and transient activity of the model in the tropics. Quart J Roy Met Soc (submitted)

Oberhuber JM (1988) An atlas based on the 'COADS' data set: The budgets of heat, buoyancy and turbulent kinetic energy at the surface of the global ocean. Max-Planck-Institut für Meteorologie, Report No 15, Hamburg, FRG

Oberhuber JM (1993a) Simulation of the Atlantic circulation with a coupled sea ice - mixed layer - isopycnal general circulation model. Part I: Model description. J Phys Oceanogr 22: 808-829

Oberhuber JM (1993b) The OPYC Ocean General Circulation Model. Deutsches Klimarechenzentrum GmbH, Technical Report No.7, Hamburg, FRG

Palmer TN, Anderson DLT (1994) The prospects for seasonal forecasting. Quart J Roy Met Soc 120: 755-793

Parker D, Jones, Folland, Bevan (1994) Interdecadal changes of surface temperature since the late nineteenth century. J Geophys Res 99: 14373-14399

Pazan SE, Meyers G (1982) Interannual fluctuations of the tropical Pacific wind field and the Southern Oscillation. Mon Wea Rev 110: 587-600

Philander SGH, Pacanowski RC, Lau NC, Nath MJ (1992) Simulation of ENSO with a global atmospheric GCM coupled to a high-resolution, tropical Pacific ocean GCM. J Climate 5: 308-329

Quinn WH, Neal VT, Antunez de Mayolo SE (1987) El Niño occurrences over the past four and a half centuries. J Geophys Res 92: 14449-14461

Rasmussen EM, Carpenter TH (1982) Variations in tropical sea surface temperature and surface wind fields associated with the Southern Oscillation/El Niño. Mon Wea Rev 111: 354-384

Robertson AW, Ma C-C, Ghil M, Mechoso CR (1995) Simulation of the tropical Pacific climate with a coupled ocean-atmosphere general circulation model. Part II:

interannual variability. J Climate 8: 1199-1216

Robock A, Mao J (1995) The volcanic signal in surface temperature observations. J Climate 8: 1086-1103

Rockel B, Raschke E, Weyres B (1991) A parameterization of broad band radiative transfer properties of water, ice and mixed clouds. Beitr Phys Atmos 64: 1-12

Roeckner E, Arpe K, Bengtsson L, Brinkop S, Dümenil L, Esch M, Kirk E, Lunkeit F, Ponater M, Rockel B, Sausen R, Schlese U, Schubert S, Windelband M (1992) Simulation of the present-day climate with the ECHAM model: Impact of model physics and resolution. Max-Planck-Institut für Meteorologie, Report No. 93, Hamburg, FRG

Ropolewski CF, Halpert MS (1987) Global and regional scale precipitation patterns associated with the El Niño/Southern Oscillation. Mon Wea Rev 115: 1606-1626

Sausen R, Barthel K, Hasselmann K (1988) Coupled ocean-atmosphere models with flux correction. Clim Dyn 2: 145-163

Sausen R, Schubert S, Dümenil L (1994) A model of river run-off for use in coupled atmosphere-ocean models. J Hydrology 155: 337-352.

Schneider EK, Zhu Z, Giese BS, Huang B, Kirtman BP, Shukla J, Carton JA (1995) Annual cycle and ENSO in a coupled ocean-atmosphere model. Center for Ocean-Land-Atmosphere Studies, Report No. 12, Calverton, USA

Sherwood SC, Ramanathan V, Tyree MK, Roeckner E (1994) Response of an atmospheric GCM to radiative forcing of tropical cirrus. J Geophys Res 99: 20829-20845

Shukla J (1991) Short term climate variability and prediction. In Proc. Second World Climate Conference. J Jager and HL Ferguson (eds), 203-210, Cambridge University Press

Slingo JM, Blackburn M, Betts A, Brugge R, Hodges K, Hoskins B, Miller M, Steenman-Clark L, Thuburn J (1994) Mean climate and transience in the tropics of the UGAMP GCM: Sensitivity to convective parameterization. Quart J Roy Met Soc 120: 881-922.

Suarez MJ, Schopf PS (1988) A delayed action oscillator for ENSO. J Atmos Sci 45: 3283-3287

Tett SFB (1995) Simulation of El Niño-Southern Oscillation-like variability in a global AOGCM and its response to CO_2 increase. J Climate 8: 1473-1502.

Trenberth KE, Shea DJ (1987) On the evolution of the Southern Oscillation. Mon Wea Rev 115: 3078-3096

van Loon H, Madden RA (1981) The Southern Oscillation. Part I: Global associations with pressure and temperature in northern winter. Mon Wea Rev 109: 1150-1162.

Wallace JM, Gutzler DS (1981) Teleconnections in the geopotential height field during the Northern Hemisphere winter. Mon Wea Rev 109: 784-812.

Williamson DL, Rasch PJ (1994) Water vapor transport in the NCAR CCM2. Tellus 46A: 34-51

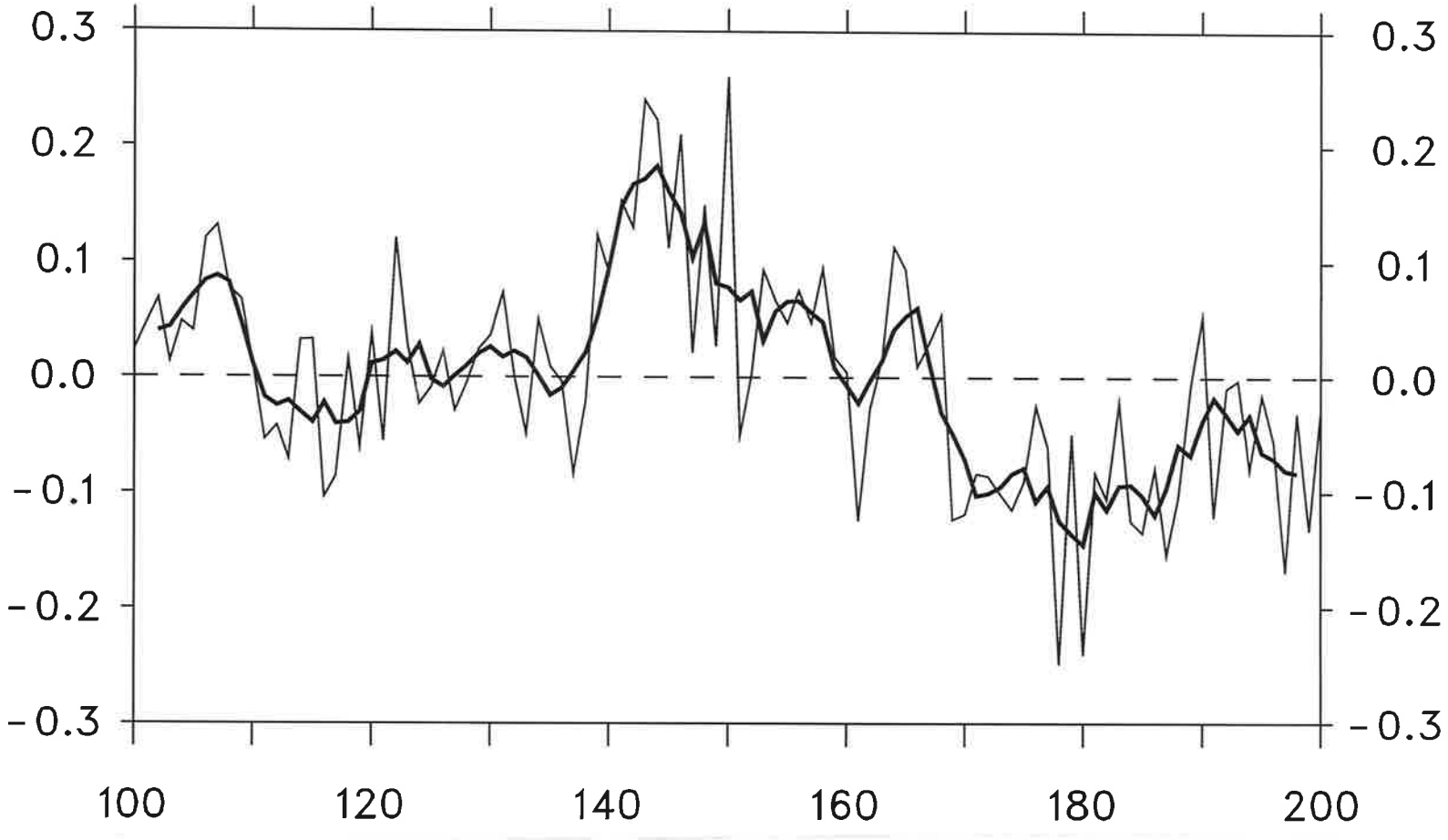

Fig. 1. Deviation of global annual mean surface air temperature (K) from the 100 year mean (14.7°C) between years 100 and 200 of the CGCM control experiment. The smoothed curve (bold) represents 5-year running means.

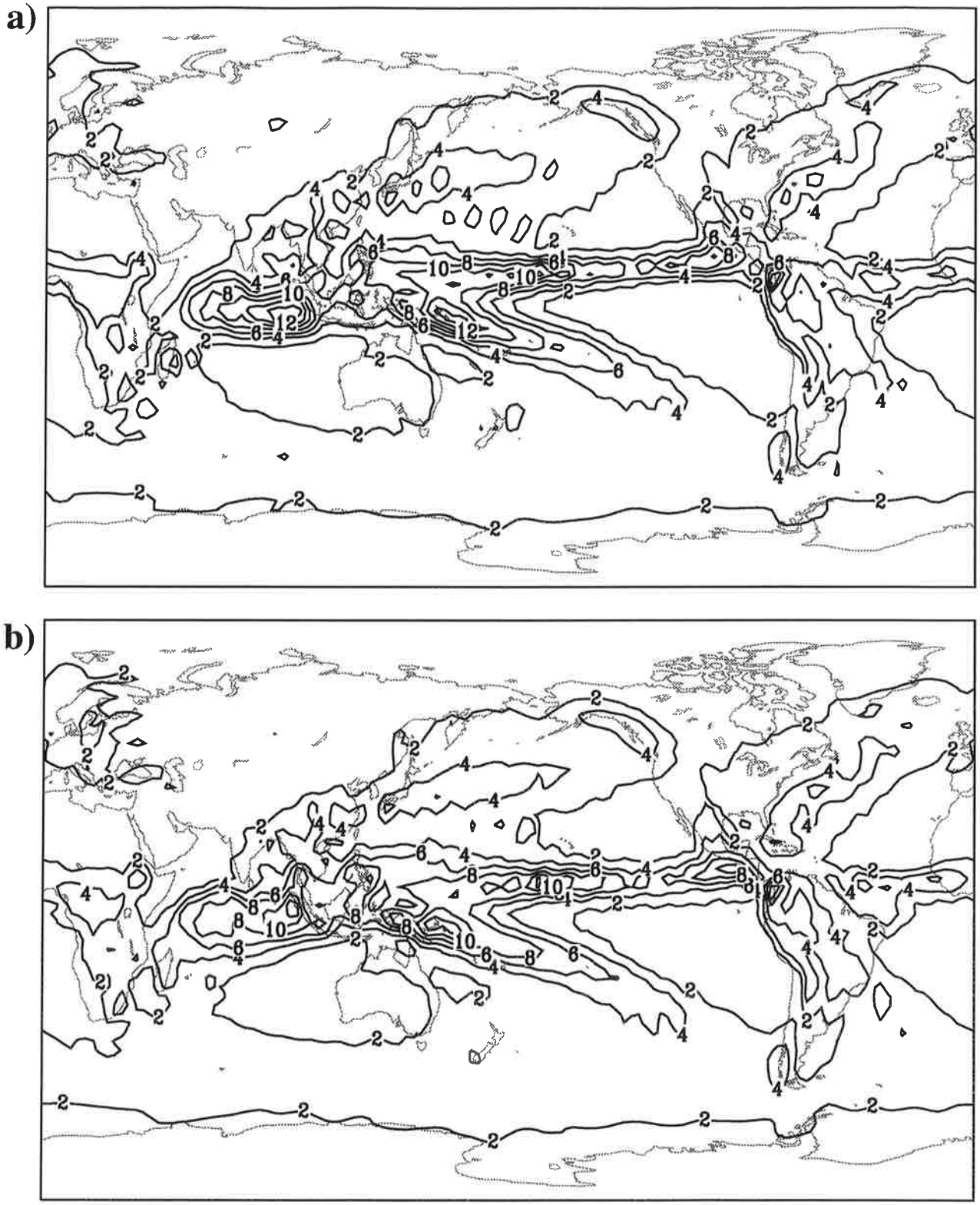

Fig. 2. Annual mean precipitation (mm/d) as simulated in the a) CGCM (50 year mean), b) ECHAM-4 forced with observed SSTs 1979-94 (mean of two realizations).

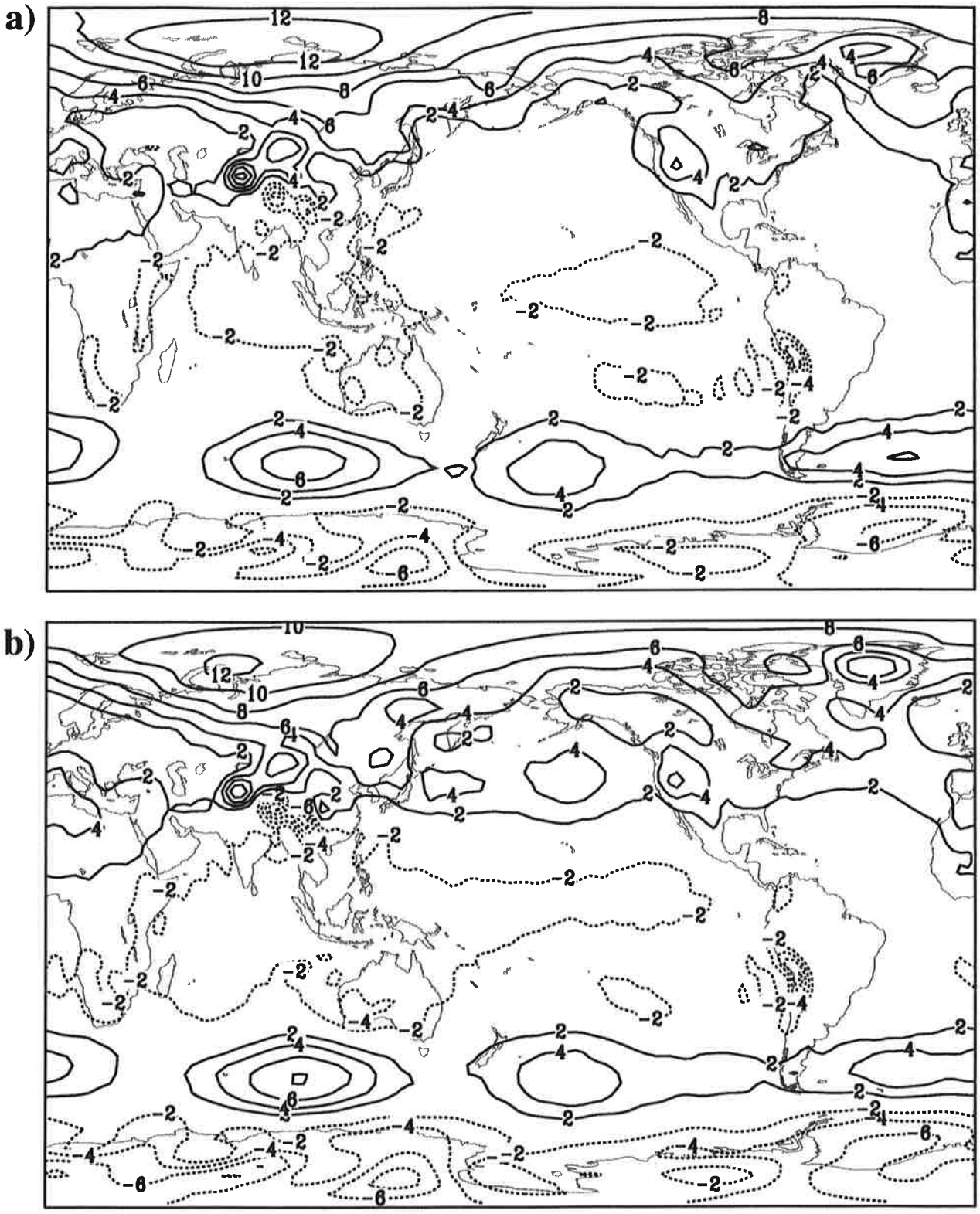

Fig. 3. Deviation of simulated DJF sea level pressure from ECMWF analyses, a) CGCM – ECMWF, b) ECHAM4 – ECMWF. Units are hPa. The zero contour line is suppressed.

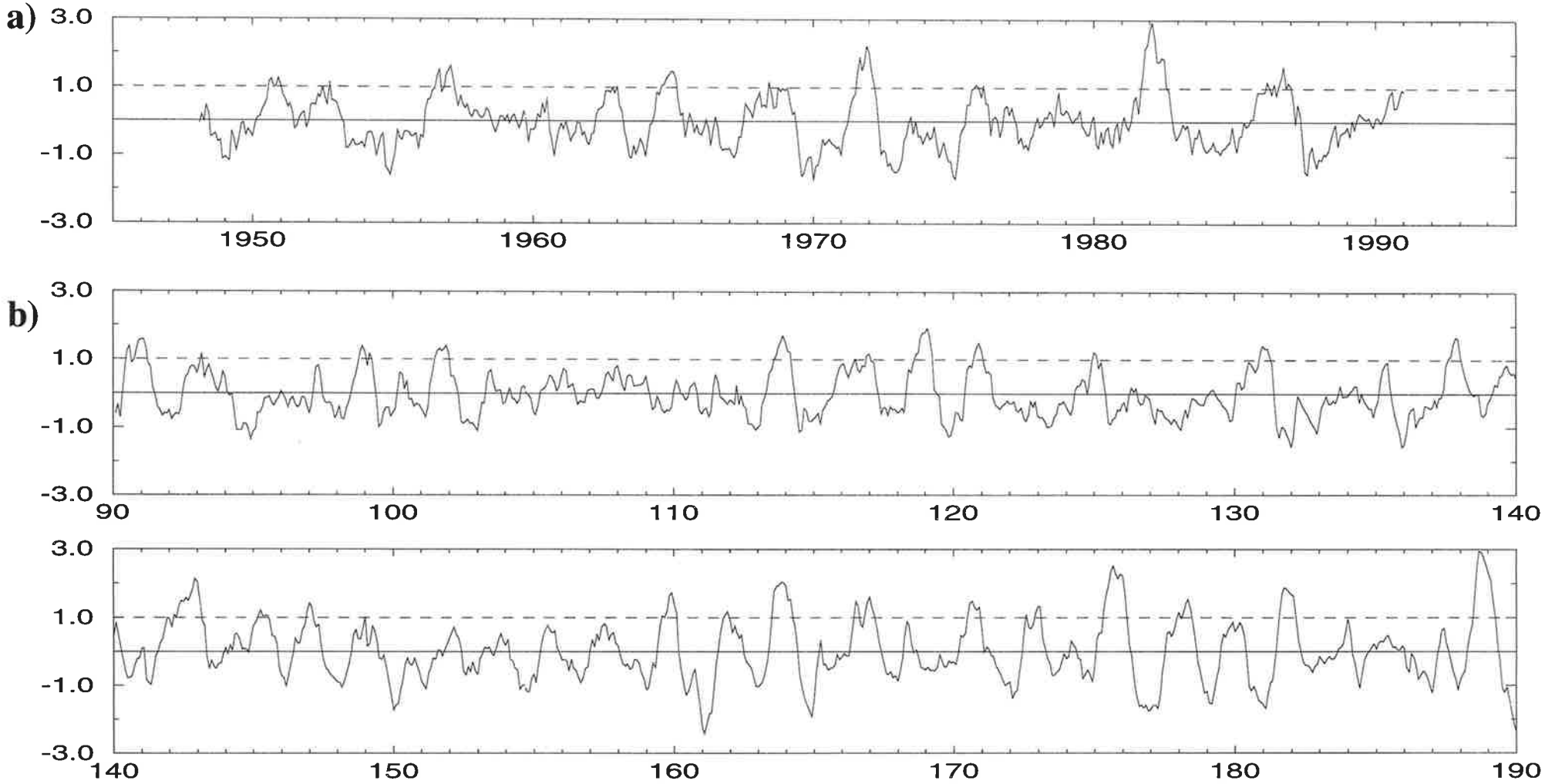

Fig. 4. Time series of SST anomalies (K) averaged over NIÑO3 region (5°N - 5°S, 90°W - 150°W): a) GISST dataset (1949 - 91), b) CGCM simulation for years 90 - 140 and 140 - 190, respectively. The time series have not been filtered or detrended.

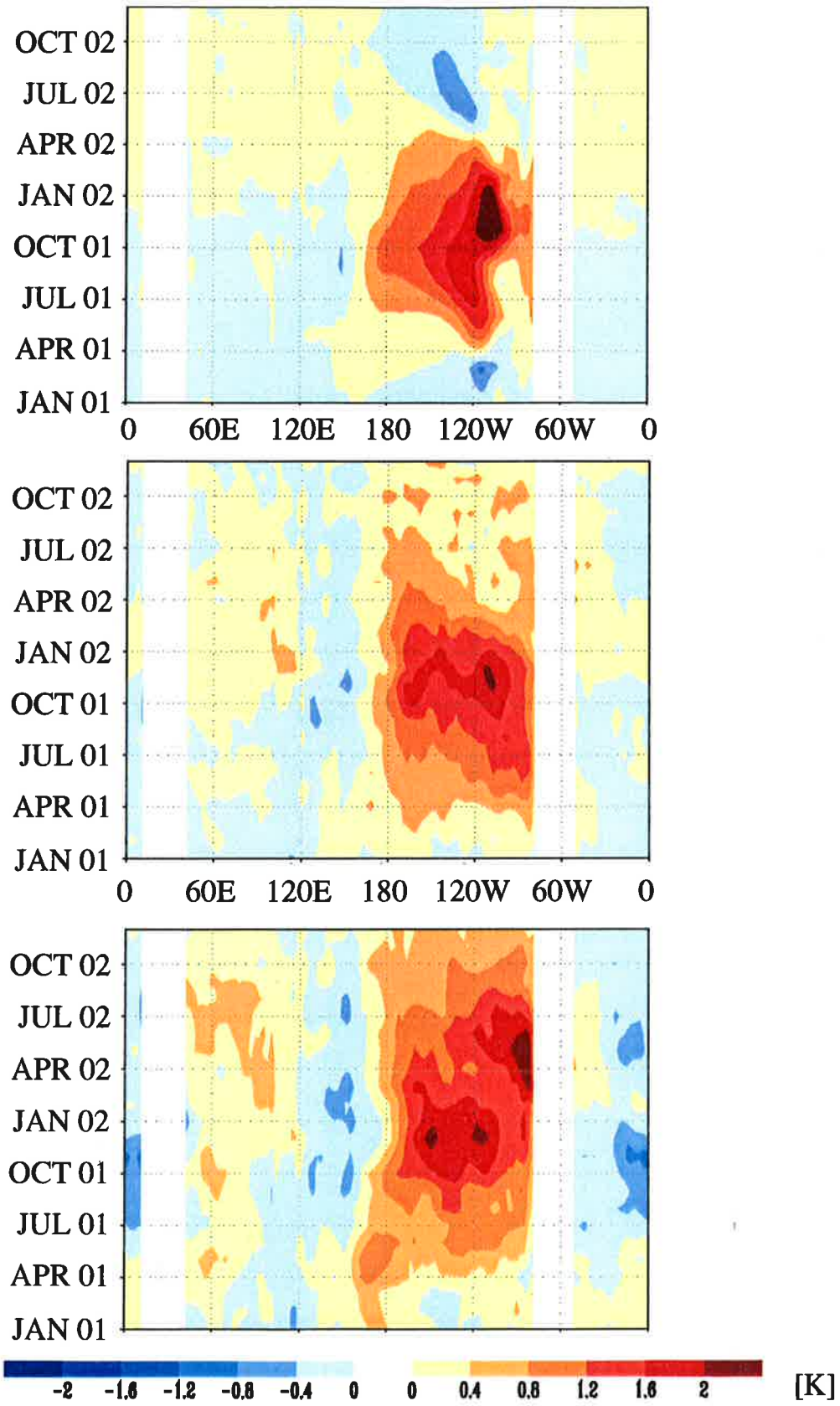

Fig. 5. Hovmöller diagrams of composite SSTA along the equatorial belt (5°N to 5°S) defined as the difference EN–NEN (year 01) and PEN–NEN (year 02), where EN, PEN and NEN denote the respective composite of El Niño, post-El Niño and non-El Niño years (see text): a) CGCM simulation (11 EN events, model years 90 - 140), b) GISST (11 EN events, 1949 - 91), c) AMIP-SST (3 EN events, 1979 - 94).

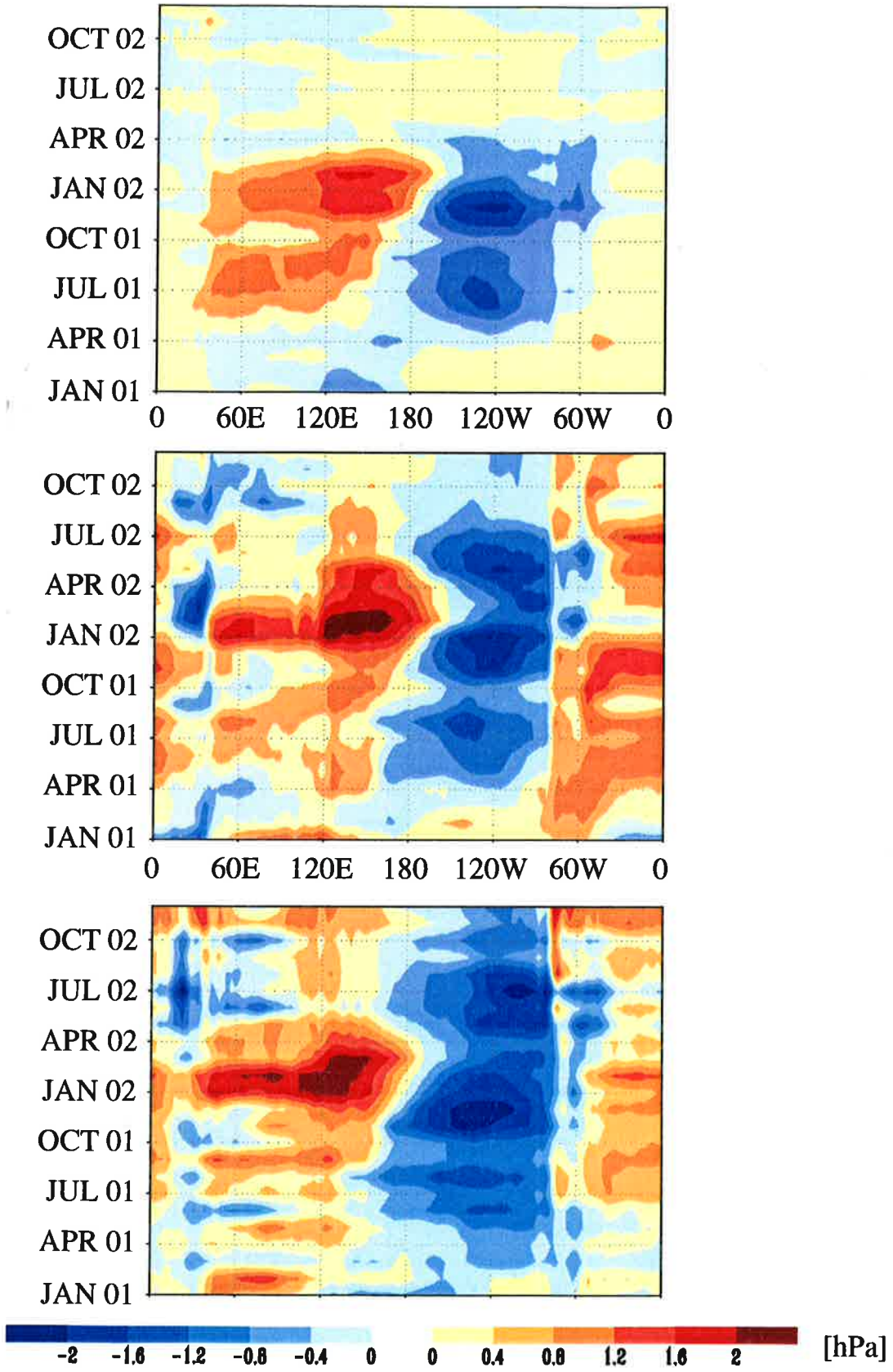

Fig. 6. Hovmöller diagrams of composite sea level pressure anomalies during EN and PEN years, respectively for a) CGCM, b) ECHAM4-AMIP (mean of two realizations), c) ECMWF analyses. For definitions of the composites see Fig. 5 and text.

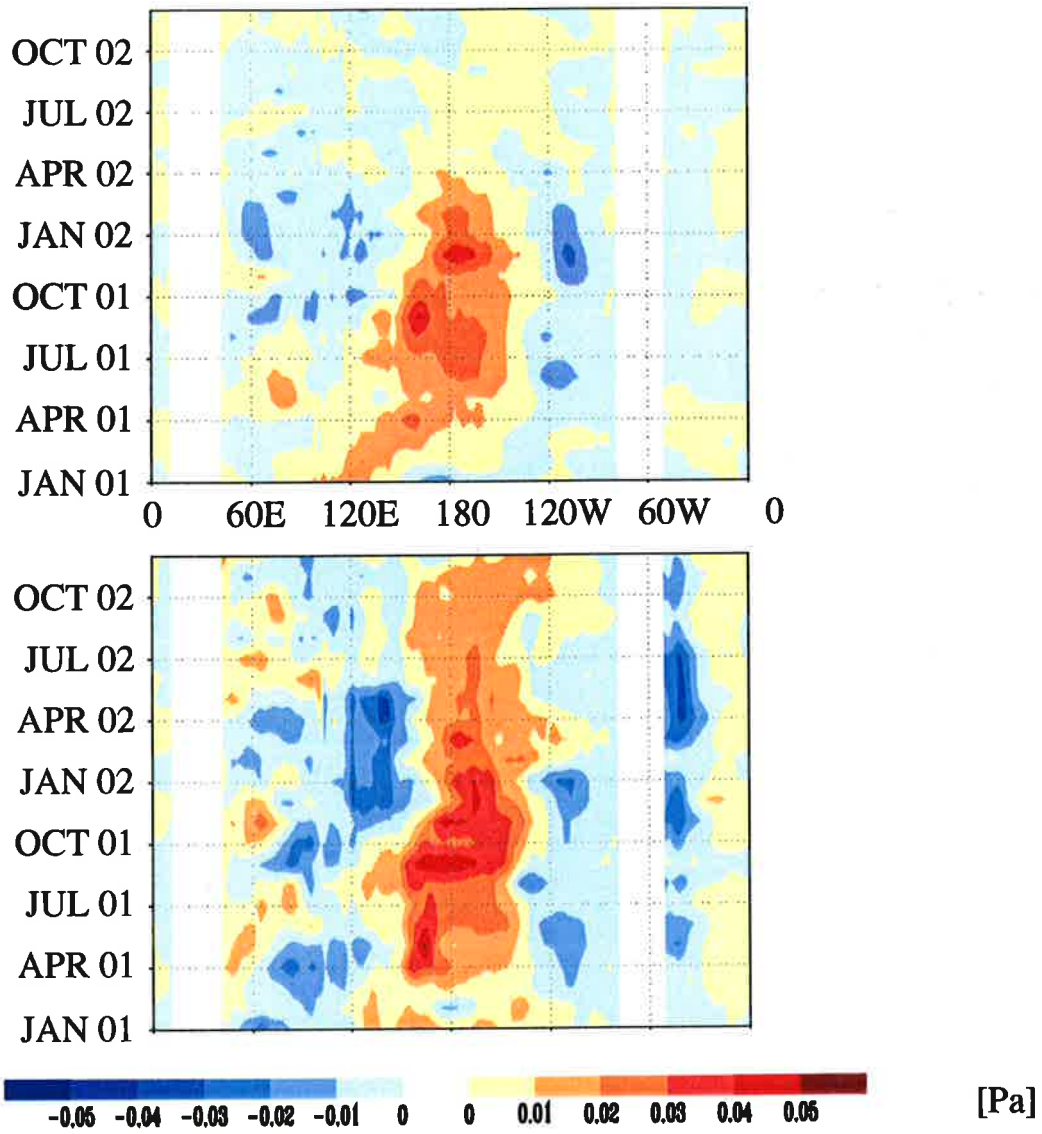

Fig. 7. Hovmöller diagrams of composite zonal wind stress anomalies during the EN and PEN years, respectively, for a) CGCM, b) ECHAM4-AMIP. For definitions of the composites see Fig. 5 and text.

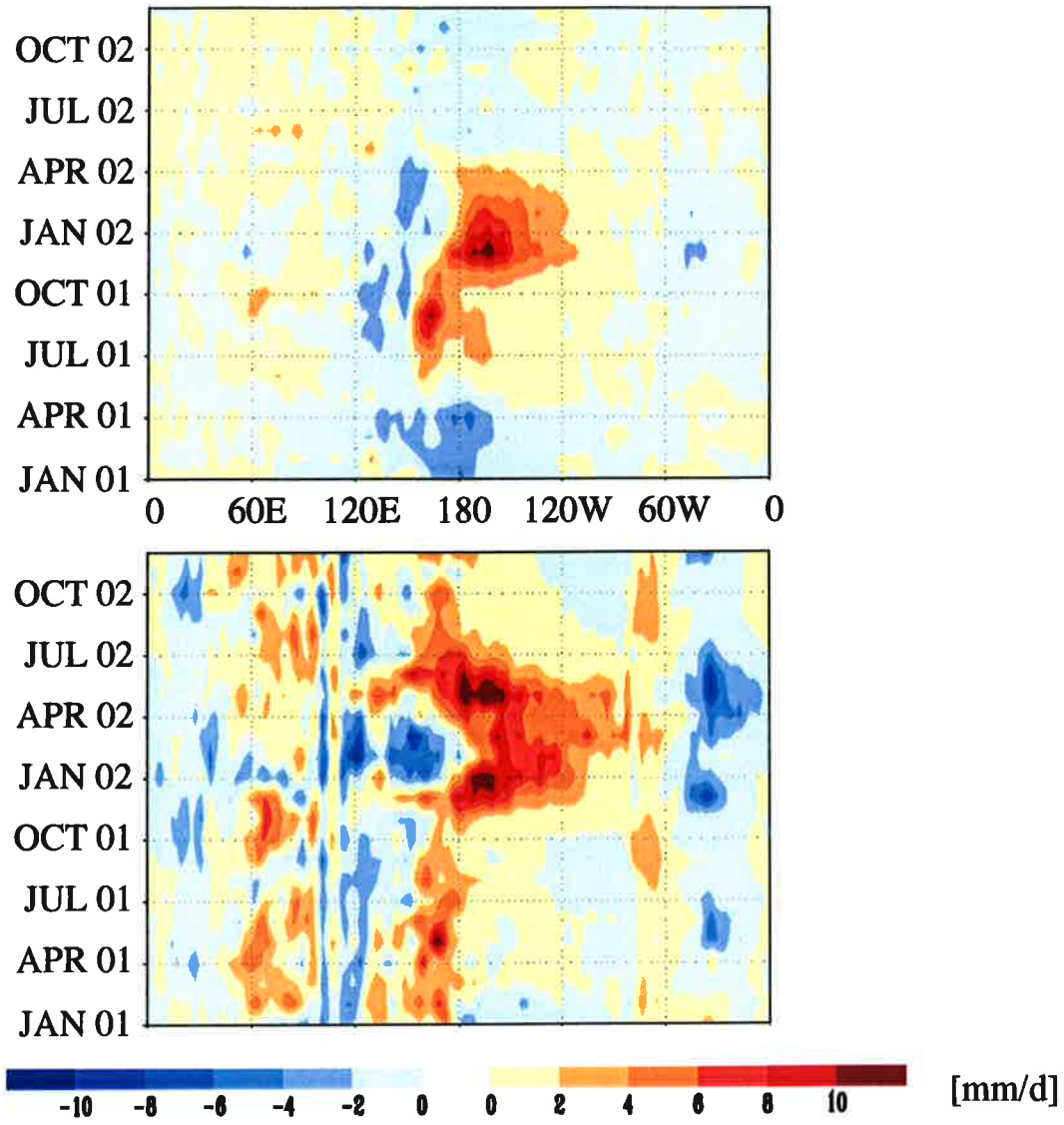

Fig. 8. Analogous to Fig. 7, but for precipitation.

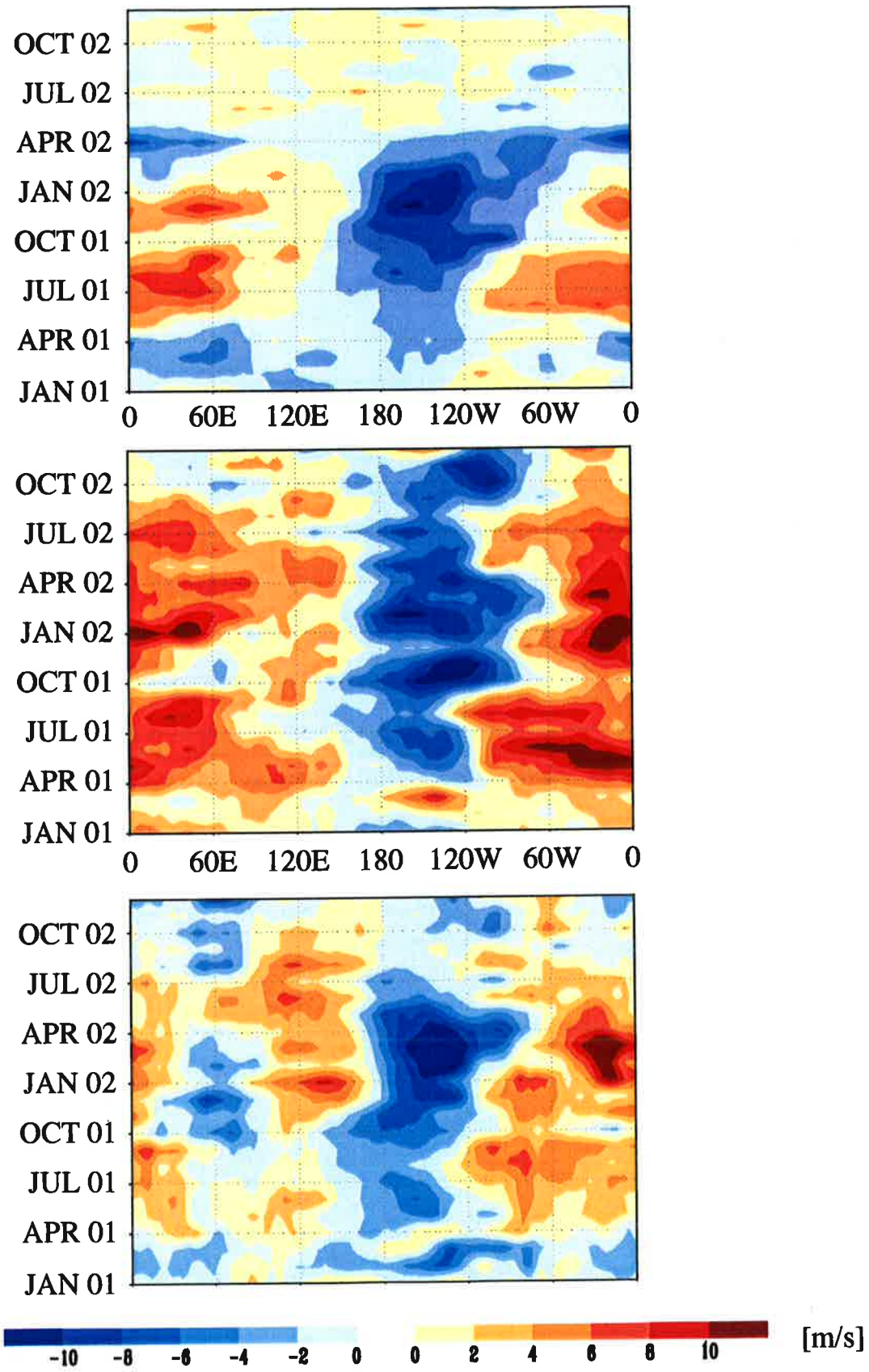

Fig. 9. Analogous to Fig. 6., but for zonal wind anomalies at the 200 hPa level.

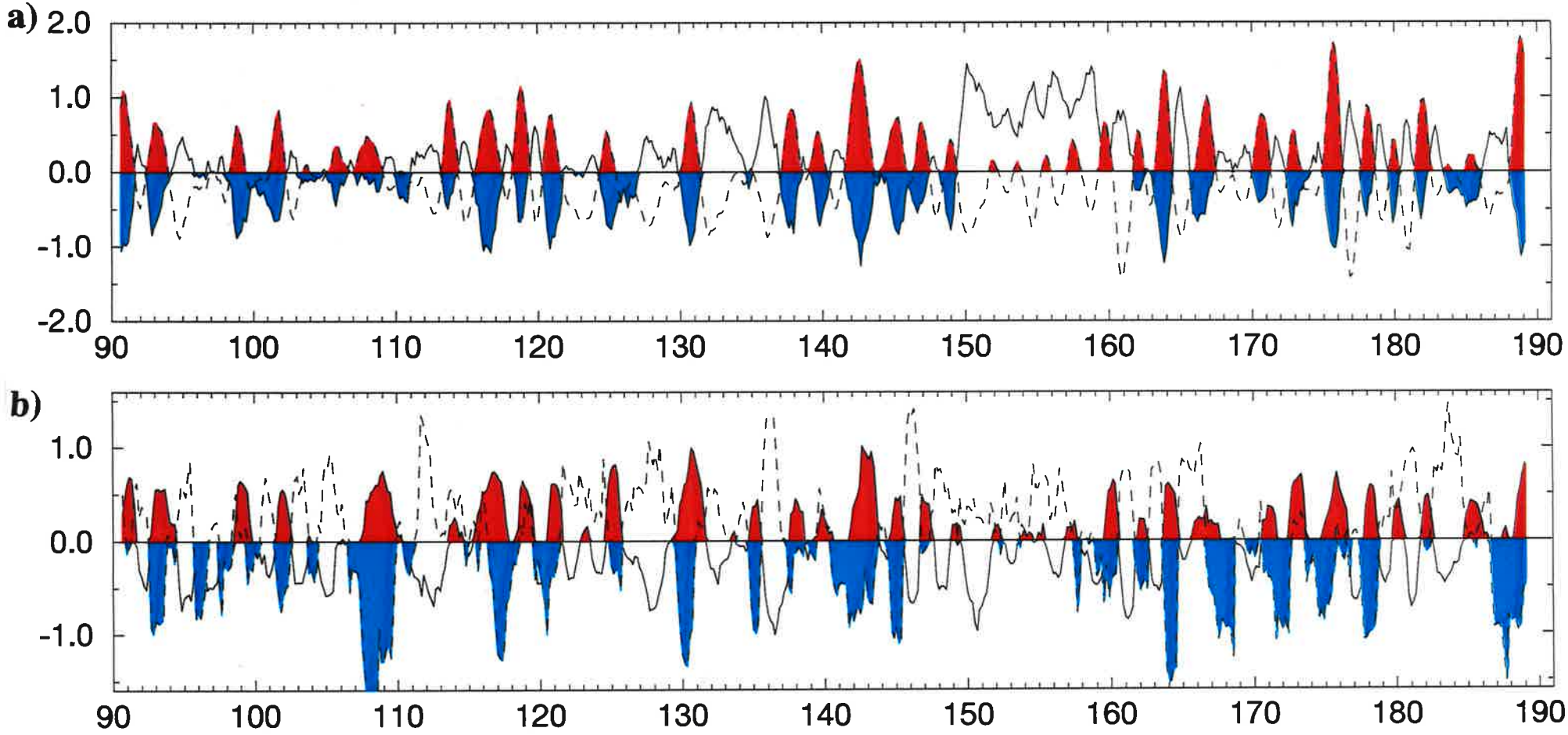

Fig. 10. Normalized index time series for years 90 to 190 of the CGCM simulation: a) NIÑO3-SSTA (dashed, positive red) and Southern Oscillation Index (SOI, solid, negative blue) defined as the sea level pressure difference between Tahiti and Darwin (nearest grid points), b) Pacific North America (PNA) index (solid, positive red) and North Atlantic Oscillation (NAO) index (dashed, negative blue) defined as the sea level pressure difference between Lisbon and Stykkisholmur, Iceland (nearest grid points). All indices are normalized with the respective standard deviations. The time series are smoothed (13-month running means) but not detrended. For correlation coefficients see Table 2.

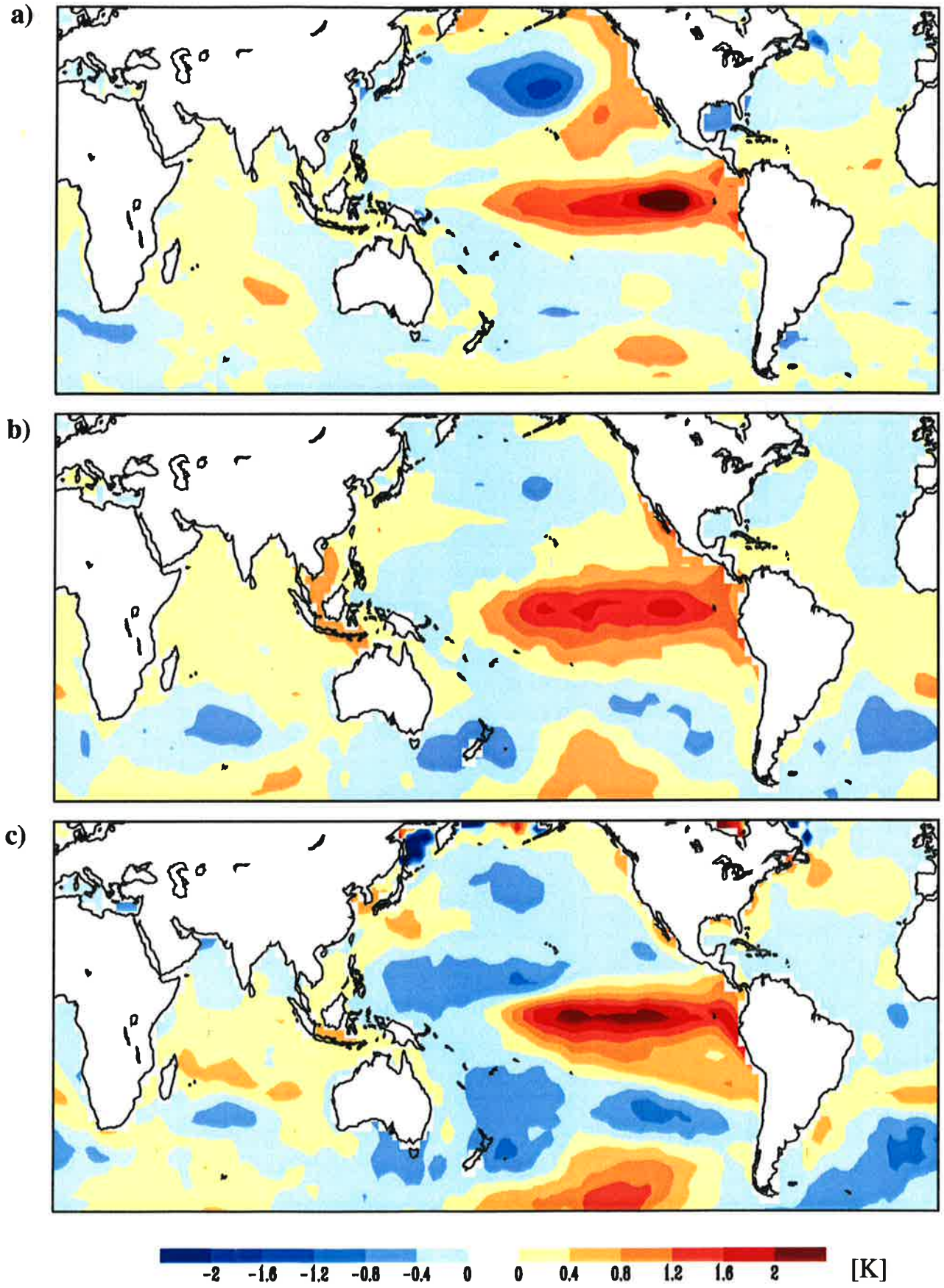

Fig. 11. Analogous to Fig. 5, but for the geographical distribution of SSTA composites (EN–NEN) during the mature stage of ENSO (DJF).

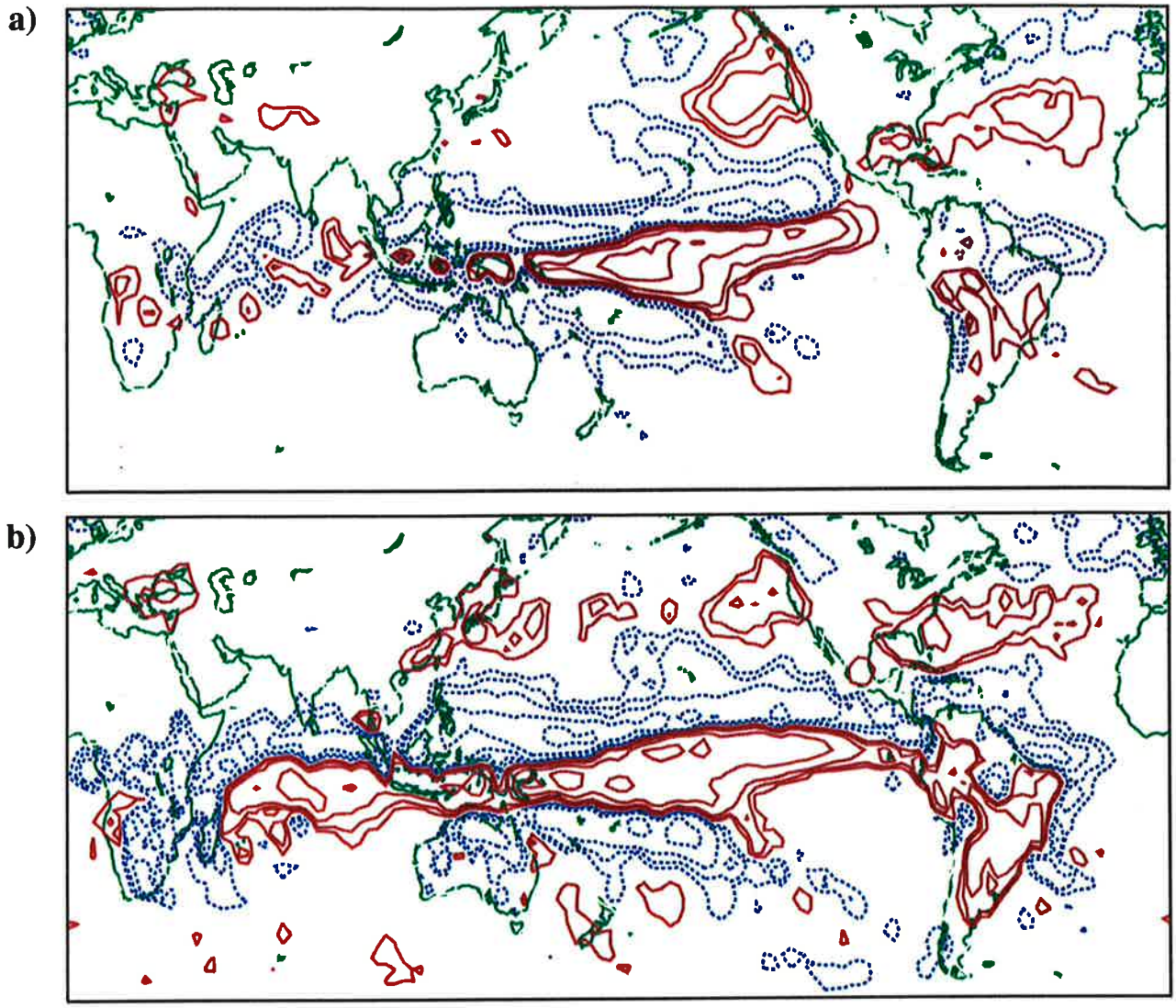

Fig. 12. Analogous to Fig. 11, but for the composite precipitation anomaly: a) CGCM, b) ECHAM4-AMIP. Contours are ± .5, 1, 2, 5, 10 mm/d with the zero line omitted. Positive anomalies in red and negative anomalies in blue.

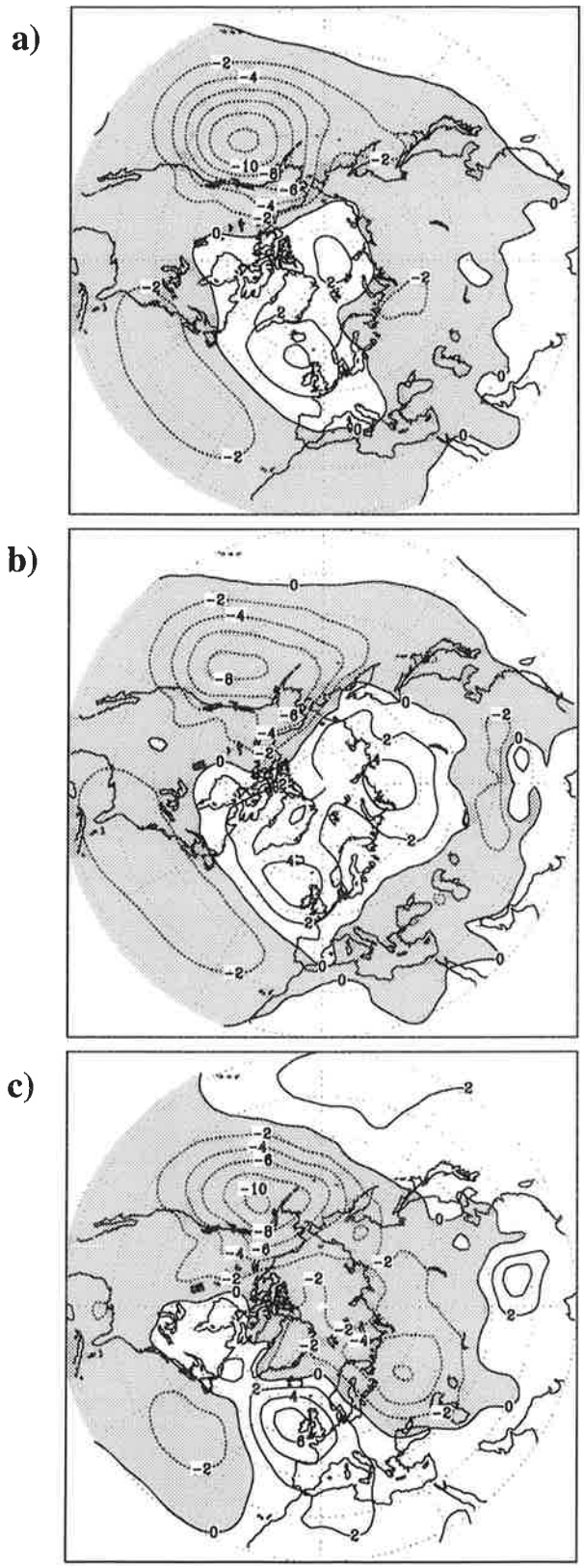

Fig. 13. The difference in sea level pressure between El Niño and non-El Niño composites during the mature stage of ENSO (DJF): a) CGCM (11 events), b) ECHAM4-AMIP (2 realizations of 3 events), c) ECMWF analyses (3 events). Contour spacing is 2 hPa and negative anomalies are shaded.

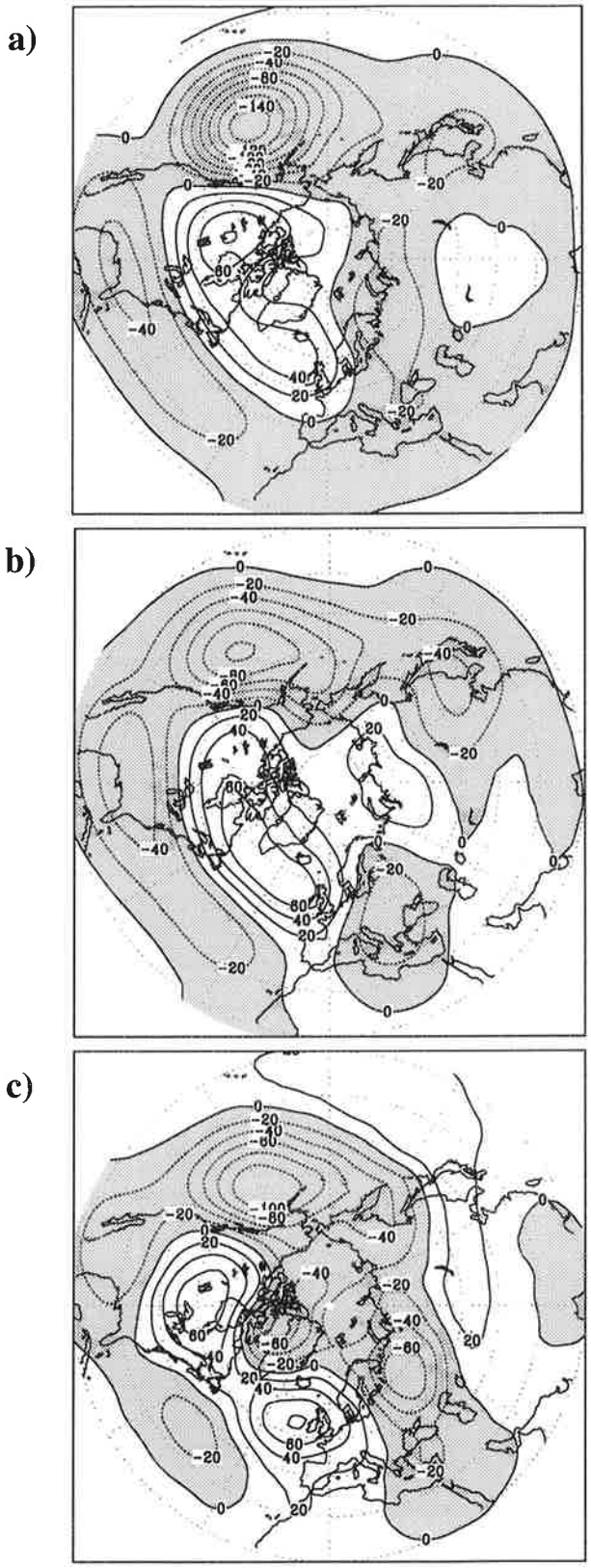

Fig. 14. Analogous to Fig. 13, but for the composite geopotential height difference at the 500 hPa level. Contour spacing is 20 gpm.

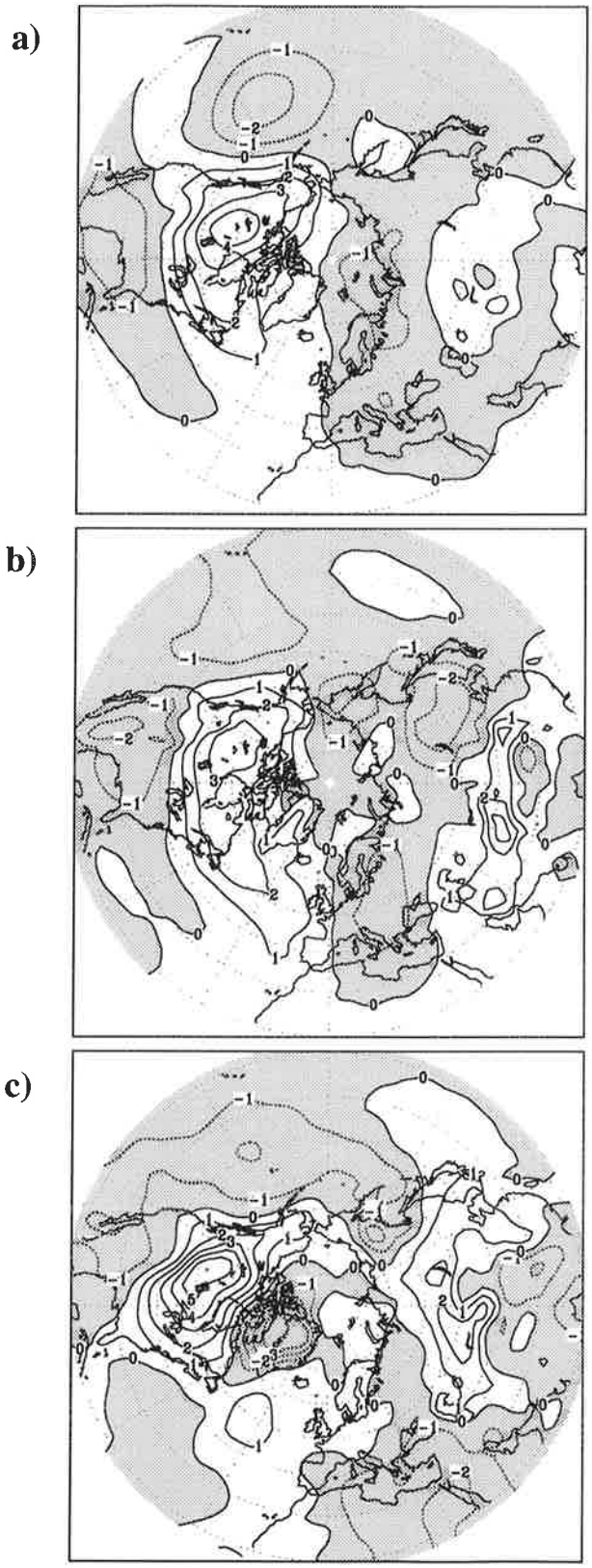

Fig. 15. Analogous to Fig. 13, but for the composite temperature difference at the 850 hPa level. Contour spacing is 1 K.